Defect-Controlled 40 Ar Diffusion-Domain Structure of White Micas from High-resolution 40 Ar/ 39 Ar Crystal-Mapping in Slowly-Cooled Muscovite

Jehiel Nteme, Stéphane Scaillet, Emmanuel Gardés, Florian Duval, Peter Nabelek, Angelo Mottolese

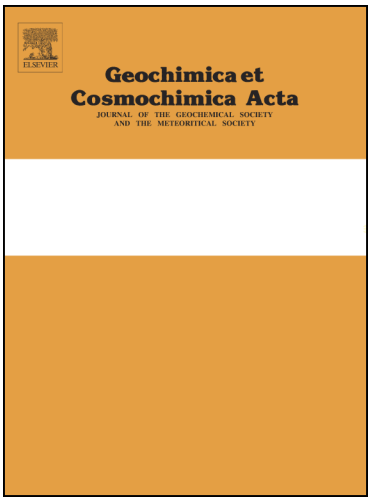

Defect-Controlled ^{40}Ar Diffusion-Domain Structure of White Micas from High-resolution ^{40}Ar/ ^{39}Ar Crystal-Mapping in Slowly-Cooled Muscovite

Jehiel Nteme, Stéphane Scaillet, Emmanuel Gardés, Florian Duval, Peter Nabelek, Angelo Mottolese

PII: S0016-7037(22)00651-2
DOI: https://doi.org/10.1016/j.gca.2022.12.004
Reference: GCA 12894

To appear in: *Geochimica et Cosmochimica Acta*

Received Date: 24 June 2022
Accepted Date: 1 December 2022

Please cite this article as: Nteme, J., Scaillet, S., Gardés, E., Duval, F., Nabelek, P., Mottolese, A., Defect-Controlled ^{40}Ar Diffusion-Domain Structure of White Micas from High-resolution ^{40}Ar/ ^{39}Ar Crystal-Mapping in Slowly-Cooled Muscovite, *Geochimica et Cosmochimica Acta* (2022), doi: https://doi.org/10.1016/j.gca.2022.12.004

Defect-Controlled ^{40}Ar Diffusion-Domain Structure of White Micas from High-resolution $^{40}Ar/^{39}Ar$ Crystal-Mapping in Slowly-Cooled Muscovite

Jehiel Nteme[a,b,*], Stéphane Scaillet[a], Emmanuel Gardés[c,d], Florian Duval[a], Peter Nabelek[e], Angelo Mottolese[a,f]

[a] *Université Orléans, CNRS, BRGM, Institut des Sciences de la Terre d'Orléans (ISTO), UMR 7327, F-45071, Orléans, France*
[b] *Now at: Université Orléans, CNRS, Groupe de Recherches sur l'Energétique des Milieux Ionisés (GREMI), UMR 7344, 45067 Orléans, France*
[c] *Centre de recherche sur les Ions, les Matériaux et la Photonique (CIMAP), Normandie Université France*
[d] *Now at: Université Clermont Auvergne, CNRS, IRD, OPGC, Laboratoire Magmas et Volcans, F-63000 Clermont-Ferrand, France*
[e] *Department of Geological Sciences, University of Missouri, Columbia, Missouri 65211, U.S.A*
[f] *Now at: Instituto de Nanociencia y Materiales de Aragón, 50009 Zaragoza, Spain*

Abstract

Using target-matching techniques combining $^{40}Ar/^{39}Ar$ crystal-mapping with elemental mapping and high-resolution electron microscopy, this study investigates the ^{40}Ar behavior in very-slowly cooled muscovite from the Harney Peak Granite (HPG, South Dakota, USA). Detailed age mapping along (001) in single crystals from different localities of the HPG documents age gradients in excess of $\sim 300-400$ m.y., with conspicuous internal $^{40}Ar/^{39}Ar$ zoning. This suggests (001) layer-parallel ^{40}Ar transport driven by diffusion, consistent with previous $^{40}Ar/^{39}Ar$ crystal-mapping studies. The age distribution pattern is complex, however, and defines a mosaic of sub-grain domains with more retentive core zones, broadly $\sim 250-300$ μm across, separated by zones of high diffusivity varying in shape and extent. The maximum ages preserved in the core domains are independent of their size but vary linearly with the bulk areal extent of the peripheral (or surrounding) high-diffusivity zones. Spatial $^{40}Ar/^{39}Ar$ relationships inside each grain point to a mechanism of multipath continuum-diffusion interaction between subdomains across the whole crystal, rather than via discrete non-interracting domains such as in K-feldspars. A close spatial correlation exists between younger ages, Na-depleted (K-enriched) zones, and density of microstructural defects. These defects, identified as lenticular voids and basal partings (< 100 nm$-$long), are developed in response to inward

*Corresponding authors
Email address: jehiel.nteme-mukonzo@univ-orleans.fr (Jehiel Nteme)

K ↔ Na interdiffusion during late-magmatic stages, in the absence of deformation. Coupled variations in density of microstructural defects and Na−K interchange are inferred to control the bulk diffusion-domain structure of HPG muscovite. Quantitative diffusion modeling of coupled compositional−defect−isotopic variations indicates that ^{40}Ar diffusivity may be enhanced by up to six orders of magnitude in defect-controlled high-diffusivity zones relative to less defective (pristine) domains. On the other hand, empirical diffusivity estimates required to preserve the core ages are commensurate with diffusion estimates independently derived from recent atomistic simulations.

Key words: ^{40}Ar diffusion, domain structure, multipath diffusion, muscovite, (001)−parallel age−mapping, FIB-STEM/TEM, Harney Peak granite

1. INTRODUCTION

Since the first laser-based ^{40}Ar/^{39}Ar age-mapping of white micas (Scaillet et al., 1990), the technique has been rarely used to map internal (within-grain) ^{40}Ar variations along the (001) direction in muscovite (Scaillet et al., 1992; de Jong et al., 1992; Hames and Hodges, 1993; Hames and Bowring, 1994; Hodges et al., 1994; Boundy et al., 1997; Hames and Cheney, 1997; Laurent et al., 2021). Most *in situ* ^{40}Ar/^{39}Ar laser work so far has been focused instead on studying textural *vs.* ^{40}Ar retention relationships to explore the role of deformation on ^{40}Ar redistribution and resetting at the grain-scale (e.g., Di Vincenzo et al., 2001, 2004, 2006; Kramar et al., 2001, 2003; Mulch et al., 2002, 2005, 2006; Mulch and Cosca, 2004; Putlitz et al., 2005; Hames et al., 2008; Wells et al., 2008; Wiederkehr et al., 2009; Rosenbaum et al., 2012; Schneider et al., 2013; Scharf et al., 2016; Fornash et al., 2016; Kellett et al., 2016; Beaudoin et al., 2020). Such relationships are commonly studied on samples cut parallel to the XZ−plane of maximum deformation and tectonic transport of the deformation ellipsoid, hence normal to the average flattening XY−plane containing the mica basal section (001). Because ^{40}Ar diffusion in mica preferentially occurs along (001) (Nteme et al., 2022, and references below), such perpendicular cuts strongly minimize the likelihood of capturing the full travel path of argon from the core to the rim in case of transport dominated by volume (lattice) diffusion. Also, this approach compromises the overall ability to resolve near-edge effects hidden under the surface cut due to shallow or

contorted grain contacts, especially in the case of complex, interlocked, textural fabrics with low-angle oblique cuts. More importantly still, $^{40}Ar/^{39}Ar$ gradients in fabric or foliation-forming micas may be locally affected by internal defects at conditions unlikely to reflect diffusion-dominated transport (Kramar et al., 2001).

The best option to study first-order argon diffusive patterns is by $^{40}Ar/^{39}Ar$ mapping along (001) in magmatic micas. Micas in plutonic rocks are early-crystallizing phases that commonly develop mm-size sub-automorphic shapes at magmatic temperatures, often with little subsequent disruption of the original grain boundaries as the host pluton cools down and crystallizes unaffected by deformation. Detailed internal 2D mapping along (001) under such auspices essentially appeared in the early 1990's at a time when the resolving power, extraction wavelength, and instrumental sensitivity and throughput did not match the current technology for within-crystal $^{40}Ar/^{39}Ar$ mapping (Phillips and Onstott, 1988; Scaillet et al., 1990, 1992; Onstott et al., 1991; Phillips, 1991; de Jong et al., 1992; Hames and Hodges, 1993; Hames and Bowring, 1994; Hodges et al., 1994; Hodges and Bowring, 1995; Kelley et al., 1994; Hames and Cheney, 1997). Despite their limitations, these studies clearly established that ^{40}Ar diffusion in micas indeed proceeds along (001) with the effective diffusion length controlled to first-order by the physical grain size. They also showed that the geometry of diffusion may be far from perfect, possibly involving internal defects such as Guinier-Preston zones in biotite and phlogopite (Onstott et al., 1991; Phillips, 1991).

Except for one occasion (Hodges et al., 1994), magmatic muscovite largely eluded the attention of early $^{40}Ar/^{39}Ar$ crystal-mapping investigations, leaving our current perception of the typology of ^{40}Ar diffusion in white micas largely shaped by tectono-metamorphic studies where primary diffusion-driven patterns are invariably obscured by deformation and recrystallization (e.g., Hames and Cheney, 1997; Kramar et al., 2001, 2003; Mulch et al., 2002, 2004, 2005, 2006; Putlitz et al., 2005; Hames et al., 2008; Beaudoin et al., 2020). Purely diffusion-driven (i.e., deformation-free) natural ^{40}Ar gradients in muscovite remain inadequately characterized today, raising the question of how to relate $^{40}Ar/^{39}Ar$ age variations documented in complex field situations to ^{40}Ar diffusivities derived from experimental (Robbins, 1972; Harrison et al., 2009), empirical (Hames and Bowring, 1994; Kirschner et al., 1996), and theoretical (Nteme et al., 2022) studies. These studies differ substantially

in terms of kinetic rates, diffusion-domain structure and geometry, with considerable uncertainty surrounding the thermal-kinetic significance one can attach to muscovite $^{40}Ar/^{39}Ar$ data in terms of cooling *vs.* (re)crystallization ages in natural settings.

In a previous work (Nteme et al., 2022), we addressed the problem of the quantitative characterization of ^{40}Ar kinetics in white micas from lattice-based Molecular Dynamics (MD) and Transition State theories (TST) and concluded that ^{40}Ar diffusion in ideal (i.e., defect-free and stoichiometrically stable) muscovite is orders of magnitude slower than predicted by experiments and field-based calibrations. In this work, we bring the study a step ahead and address the case of ^{40}Ar diffusion in natural igneous muscovite grains that fulfil the condition of not having been at all or significantly deformed. Inspired by the few precedents of 2D mapping of igneous micas (Hames and Hodges, 1993; Hames and Bowring, 1994; Hodges et al., 1994; Hodges and Bowring, 1995), we selected as natural target the Harney Peak Granite in the Paleoproterozoic Black Hills of South Dakota, USA, for which prior $^{40}Ar/^{39}Ar$ regional data document protracted cooling over hundreds of million years both in the pluton and its aureole as a result of long-term stagnation in the mid-crust and progressive exhumation between ∼1600-1250 Ma (Holm et al. 1997; Dahl and Foland, 2008).

Very slow (∼ 0.5 °C/Myr) subsolidus cooling across this interval produced mm-size age gradients along (001) within individual mica crystals, in a context akin to a "natural" diffusion experiment optimal for investigating the ^{40}Ar diffusion mechanisms in undeformed muscovite with a resolution never approached before. Using target-matching techniques combining extensive $^{40}Ar/^{39}Ar$ crystal-mapping with high resolution electron microscopy imaging and elemental mapping, our study documents fundamental compositional and crystal-structural effects controlling the defect and diffusion-domain structure of muscovite. These are described and quantitatively integrated in a numerical model of defect-controlled multi-path ^{40}Ar diffusion-domain behavior that is applicable to other settings as well.

2. GEOLOGICAL SETTING

The Harney Peak granite (HPG) is a peraluminous leucogranite located in the south-central portion of the Proterozoic core of the Black Hills, South Dakota (Fig. 1). It is hosted by regionally metamorphosed sedimentary rocks affected by staurolite to sillimanite-grade

metamorphism. The HPG consists of a large central pluton with smaller satellite granitic and pegmatitic plutons. The main pluton and the satellite intrusions have domal structures consisting of hundreds of sills. According to Duke et al. (1988), the HPG grew upward and outward by successive intrusions of new sills at the periphery of earlier intrusions. The magma injected during each pulse was initially homogeneous and underwent differentiation into 0.1 to 2.0 m-thick layers of Na-rich aplites and K-rich pegmatites. The mineralogy of the HPG is composed dominantly of albite, orthoclase or microcline, quartz and muscovite. Accessory minerals include biotite, tourmaline and garnet. Biotite and tourmaline are mostly mutually exclusive, the first being dominant in the core of the main pluton and the latter at the periphery and in satellite plutons.

The HPG pluton was emplaced at the culmination of the Yavapai (N-S compression) and Black Hills (E-W compression) orogenic sequence, the latter from collision of the Superior and Wyoming cratons at the southeastern extent of the earlier Trans-Hudson Orogen (Fig. 1; Dahl et al., 1999; Chamberlain et al., 2003; Dahl and Foland, 2008). The Black Hills orogeny resulted in N-S directed foliation that dominates the structural fabric of the Black Hills. The beginning of the collision is dated at $\sim$ 1750 Ma (U-Th-Pb on monazite inclusions within metamorphic garnet; Dahl et al., 2005). A range of ages is associated to the formation of the HPG: 1728 $\pm$ 4 Ma (two highly discordant U/Pb zircon ages; Redden et al., 1990), 1715 $\pm$ 3 Ma (concordant U/Pb monazite age from a thin granite sill in metamorphic rocks; Redden et al., 1990), 1711 $\pm$ 21 Ma (Rb-Sr whole-rock age, recalculated by Krogstad and Walker (1994) from Riley (1970)), and 1704 to 1700 Ma (U/Pb apatite ages from the Tin Mountain pegmatite, west of the HPG; Krogstad and Walker, 1994). This range either reflects variable discordance with U/Pb re-equilibration or mineral-specific post-crystallization cooling (monazite), in any case placing the most probable range of intrusion-crystallization ages between 1700$-$1720 Ma, possibly including overlapping of multiple intrusions in this interval as well. Collectively, the range of published ages indicates that intrusion of the HPG was the terminal stage of the $\sim$50 Myr long Yavapai - Black Hills orogenic sequence, consistent with its undeformed state.

HPG liquidus temperature from stable isotope oxygen equilibria in magmatic phases is estimated at $\sim$ 800 °C (Nabelek et al., 1992b). Intrusion probably occurred during uplift

(Nabelek and Chen, 2014) and continued until final emplacement pressure around 3.5 - 4 kbar. Post-intrusion cooling is constrained by muscovite Rb/Sr ages in the granite (Riley, 1970; Ratté, 1986; Krogstad and Walker, 1994), and $^{40}Ar/^{39}Ar$ ages on hornblende, biotite and muscovite mostly across the regional contact aureole (Berry et al., 1994; Dahl et al., 1999; Holm et al., 1997; Dahl and Foland, 2008). These data indicate relatively rapid pluton cooling through 500 °C isotherm, followed by extremely slow (< 0.5 °C/Myr) sub-solidus regional cooling characterized by hundreds of millions of years of tectonic stability in the midcrust (Holm et al., 1997; Dahl and Foland, 2008). The granite and its country rocks were ultimately uplifted during the 80−50 Ma Laramide orogeny (Lisenbee, 1978).

3. SAMPLE SELECTION AND DESCRIPTION

Muscovite crystals were obtained from five samples collected from different parts of the intrusive complex (Fig. 1). The samples were originally described in Nabelek et al. (1992a). A summary of the salient petrographic and mineralogic features is given in Table 1. Samples HP-10D and HP-13A were collected from the central pluton while HP-34C, HP-45B, and HP-2A are peripherally located in three distinct western, eastern, and northern satellite plutons, respectively. This choice was dictated by the need to account for potential age variations inside the composite pluton (Scaillet et al., 1996).

The selected samples show a common mineral assemblage dominated by quartz, K-feldspar, muscovite, and tourmaline. A few rare garnet crystals occur in HP-2A and HP-45B. In general, samples from the central facies display fine to coarse-grained granitic textures, while those of the peripheral plutons show textures ranging from aplitic to pegmatitic. Samples from the central pluton (HP-10D and HP-13A) consist of mm-size grains (Fig. 2a, b, d, g). Quartz is sub-rounded and evenly distributed. Albite and K-feldspar occur as sub-automorphic crystals, generally devoid of inclusions (Fig. 2g). Tourmaline is mm-size but can be locally larger. Muscovite often occurs as single isolated crystals, but locally forms monomineralic aggregates (Fig. 2b). While most of the muscovite grains are automorphic, some show concave edges and symplectitic texture probably due to magmatic resorption (Fig. 2d).

Sample HP-34C (peripheral pluton) contains mm- to cm-size grains. The paragenesis is

dominated by K-feldspars and quartz. Muscovite is present but with low modal proportions compared to centrally located samples. K-feldspar is also distinct from the central facies by being richer in inclusions (mainly muscovite, Fig. 2h). As in the central pluton, muscovite is often resorbed (Fig. 2e). Sample HP-45B (eastern peripheral pluton) exhibits a coarse-grained texture. Feldspars are rich in muscovite inclusions. Primary muscovite occurs as single isolated crystals displaying similar resorption characteristics. Sample HP-2A (northern satellite pluton) displays a porphyritic texture dominated by feldspar megacrysts set in a medium-grained quartz mesostasis. Muscovite often occurs as aggregates (Fig. 2c) locally exhibiting resorption patterns (Fig. 2f).

4. ANALYTICAL TECHNIQUES

4.1. In situ $^{40}Ar/^{39}Ar$ dating

After gentle crushing with a hand-held hammer, individual muscovite grains ($\geq$ 1 mm) were hand-picked under a binocular microscope based on automorphic shape, lack of visible alteration, and sharpness of grain edges. This last criterion was not met by all crystals with some grains exhibiting broken cleavage planes indicated by minor delamination locally affecting the crystal rims (Fig. 3). The selected grains were ultrasonically bathed in ethanol and deionized water for 30 s and 60 s, successively, then dried in a 50 °C oven. After microscopic examination and imaging, they were wrapped in aluminum foil, stacked in an irradiation can with sanidine monitor FCS (28.02 $\pm$ 0.28 Ma, Renne et al., 1998) interspersed every five samples and irradiated for 20 h in the CLICIT position of the Oregon State University Radiation Center (USA). After irradiation, the grains were loaded into an ultra-high vacuum laser port and baked for $\sim$ 60 hours at $\sim$ 200 °C to remove absorbed atmospheric Ar and reduce the blanks.

$^{40}Ar/^{39}Ar$ *in situ* ages were measured along the (001) cleavage plane, identified as the preferential plane of ^{40}Ar diffusion in mica (biotite and phlogopite: Giletti et al., 1974; Phillips and Onstott, 1988; Hodges and Bowring, 1995; white mica: Scaillet et al., 1990; Hames and Bowring, 1994; Nteme et al., 2022). A high-resolution deep 213-UV laserprobe (Teledyne® CETAC Technologies LSX-213G2+) was used to excavate 35 μm wide cone-shaped ablation pits about 30-40 μm deep (Fig. 4) at a repetition rate of 20 Hz and 4-5 mJ/pulse. Thirty-

four to more than one hundred fifty-six ablation spots were excavated per grain to ensure reasonably well resolved intracrystalline $^{40}Ar/^{39}Ar$ gradients in the range of the age variations recorded. The extracted gases were purified for 6 min using two air-cooled GP50 SAES getters at 250 °C equipped with two Ta-filaments held at 1500 °C, and a thermoregulated cold trap held at -127 °C before admission into one of the three static noble gas Helix-SFT (Thermo Scientific®) mass-spectrometers operated at ISTO with a mass resolution in excess of 750. Ar isotopes were measured along with ^{35}Cl by peak jumping in 10 cycles of 70 s duration with an electron multiplier (^{35}Cl, $^{36,37,38,39,40}Ar$) and a 10^{12} Ω feedback resistor-fitted Faraday cup (^{40}Ar only). Gas handling and mass-spectrometer operations are fully automated using LabView®-based in-house software. Procedural blanks were monitored before every sample gas admission in the same conditions as the unknowns. Typical values were 0.1-0.05 fA and ∼ 0.001 fA for $m/e = 40$ and $m/e = 39, 38, 37, 36$, respectively. Data regression and age calculations were applied following Scaillet (2000). Regressed $^{40}Ar/^{39}Ar$ isotopic data are tabulated in **Supplementary Material A**. Individual age errors are quoted at ± 1σ and include propagation of all instrumental and procedural uncertainties. Further technical details can be found in Beaudoin et al. (2020) and Laurent et al. (2021).

4.2. Microchemistry and high-resolution electron microscopy

Muscovite composition was investigated in thin sections with an electron microprobe (EMP) CAMECA® SX FIVE using a 15 keV and 6 nA beam at ISTO. The surfaces of some grains initially analyzed by $^{40}Ar/^{39}Ar$ were mapped with energy-dispersive X-ray spectroscopy (EDS) using a 30 keV and 3.2 nA beam in a scanning electron microscope coupled with focused Ga-ion beam and scanning transmission electron detector (SEM-FIB-STEM) FEI Helios Nanolab® 660 at CIMAP. EDS chemical compositions are computed and internally calibrated via the proprietary Aztec® EDS acquisition and data processing software (Oxford Instruments).

Microstructure was investigated on $^{40}Ar/^{39}Ar$ dated and chemically mapped grains using transmission electron microscopy. Ion-thinned, ∼100 nm-thick lamellas (FIB foils) were extracted perpendicularly to the surface of selected samples, i.e., perpendicularly to (001) plane, using the SEM-FIB-STEM. They were imaged using the SEM-FIB-STEM operated

at 30 keV and via transmission electron microscopy (TEM) with a JEOL 2010F® model operated at 200 keV.

5. *IN SITU* ^{40}Ar/^{39}Ar MAPPING RESULTS

In situ ^{40}Ar/^{39}Ar mapping was performed on all individual grains, including two split pairs obtained by cleaving individual mica flakes (muscovite *M19* and *M21* of HP-13A). This was done in order to check for intra-sample variations in diffusive behavior at the scale of different flakes ($\sim$ 50 μm thick) within the same mica specimen. Ablation pits are not systematically distributed over the same (topmost) surface layer on all samples. Some analyzes were also obtained on planes locally exposed underneath due to peripheral delamination (mechanical splitting) during extraction (cf. Fig. 4). The *in situ* data are presented as apparent age maps interpolated between ablation pits using the Kriging interpolation option of Surfer® 13 software. The overall age distribution at the scale of each individual grain is displayed as a stacked probability density plot (probability density distribution plot, PDD, or ideogram, cf. Deino and Potts, 1992) constructed by summing the individual Gaussian densities of each analysis and normalizing to the total number of spots included. Also, PDD are compared with the age frequency curve integrated from the ^{40}Ar/^{39}Ar scalar field interpolated across the pointwise data distribution for each grain and computed over of 100,000 to $\sim$ 500,000 points according to the crystal size (labelled "IAF", for Interpolated Age Frequency). Tabulated data and figures showing the location of the ablation pits inside each crystal are provided in **Supplementary Material A**. In what follows, individual crystals from the same sample are designated with their respective label (e.g., muscovite *M3* of sample HP-10D) as reported in the plots, along with their split number #, where applicable.

5.1. Sample HP-10D (Central pluton)

HP-10D (M3): $N = 57$ *in situ* ^{40}Ar/^{39}Ar ages were extracted that range from 1.3 to 1.7 Ga. The PDD and the IAF spectra show a dominant mode between 1.60 and 1.65 Ga and some smaller peaks of younger age (Fig. 5a). The age map reveals two older cores approximately 350 and 500 μm across surrounded by younger ages ($<$ 1.45 Ga) located mainly in the lower left corner of the grain in the orientation displayed.

HP-10D (M9): $N = 126$ ages were obtained between 1.28 and 1.73 Ga. These were measured mainly on the topmost surface plane, but also include data from layers exposed underneath by peripheral delamination. The PDD curve shows a dominant peak at 1.60 Ga and another at 1.40 Ga (Fig. 5b). The IAF curve shows a similar distribution, with a more prominent peak at 1.40 Ga. The age map reveals concentric gradients with a gradual core-to-rim younging except for the rightmost crystal side, delineating three broad sub-grain domains (coined "sub-domains" for short hereafter).

HP-10D (M10): $N = 104$ ages measured on the same cleavage plane are comprised between 1.30 and 1.72 Ga. The PDD curve shows a dominant peak at 1.4 Ga and a secondary one between 1.60 and 1.65 Ga (Fig. 5c). The IAF curve reproduces the same peaks with an additional one at 1.5 Ga. The age map reveals two broadly concentric core zones preserving ages older than 1.55 Ga separated by a relatively narrow zone of younger ages between 1.50 and 1.45 Ga. Ages younger than 1.40 Ga are mostly located on the rims but also predominate over a large area at the top left corner of the grain.

HP-10D (M11): The $N = 93$ data range from 1.30 to 1.73 Ga. The PDD and IAF curves reveal an age distribution similar to HP-10D (*M3*) with a dominant peak at 1.65 Ga and younger maxima (Fig. 5d). Again, a concentric core-to-rim rejuvenation is seen with the age gradient locally disturbed by zones of younger ages delineating two sub-domains, 350 to 500 μm across.

5.2. Sample HP-13A (Central pluton)

HP-13A (M3): $N = 130$ spots measured on different cleavage planes (levels) range from 1.20 to 1.70 Ga with similar PDD and IAF curves showing a dominant peak at 1.50 Ga (Fig. 6a). A rim-ward rejuvenation pattern is seen with two cores featuring ages older than 1.55 Ga. Most of the ages younger than 1.45 Ga are from lower layers exposed in peripheral (delaminated) areas.

HP-13A (M18): The $N = 128$ spot data range from 1.30 to 1.70 Ga with a more complex PDD pattern showing a dominant peak at 1.60 Ga followed by a younger one at 1.40 Ga (Fig. 6b). The IAF curve shows a similar distribution. These are again associated to concentric core-to-rim younging gradients with irregularly shaped younger zones (< 1.45 Ga) runing across the crystal and isolating two sub-domains.

HP-13A (M19): Two splits (#1 and #2) were mapped in detail. Split #1 (N = 123) covers the range 1.30-1.63 Ga with scattered peaks at 1.40, 1.45, and 1.55 Ga (revealed both by the PDD and IAF curves; Fig. 6c). Split #2 (N = 101) ranges from 1.30 to 1.61 Ga with two well-resolved peaks at 1.55 and 1.40 Ga (Fig. 6d). Age maps of both splits define a broadly similar island-and-trough distribution, with younger ages isolating up to three cores with a characteristic dimension of 400-500 μm (Fig. 6c, d).

HP-13A (M21): Two splits (#1 and #2) were mapped in detail. Split #1 (N = 102) returned a range between 1.30 and 1.72 Ga. The PDD and the IAF plots show a dominant peak at 1.65 Ga (Fig. 6e). In Split #2, ages (N = 113) range from 1.67 and 1.30 Ga. The PDD and the IAF spectra reveal two peaks at 1.65 and 1.45 Ga (Fig. 6f). The age maps show quite markedly different distributions between both splits, with two older concentric cores in Split #1, ~500 μm across, surrounded by younger ages near the rims. The rightmost core appears truncated by the rim, presumably as a result of sample comminution during extraction (Fig. 6e). Split #2 also shows a younging towards the rims but with younger ages < 1.45 Ga distinctly organized in a channel-shaped zone separating the crystal into two parallel subdomains (Fig. 6f).

5.3. Sample HP-45B (Eastern peripheral pluton)

HP-45B (M8) has been mapped in detail with N = 119 spots on different planes exposed across the external surface. Ages range from 1.25 to 1.73 Ga, the majority being comprised between 1.30 and 1.60 Ga. The PDD curve displays a broad peak extending from 1.35 to 1.55 Ga (Fig. 7a). The IAF curve shows a dominant peak at 1.35 Ga. The age map shows a systematic younging towards the rims and a broad central zone of older ages arranged diagonally across the crystal.

5.4. Sample HP-2A (Northen peripheral pluton)

N = 28 ablations in crystal *M6* returned ages between 1.25 and 1.55 Ga with a dominant peak at 1.40 Ga (in both PDD and IAF curves) and a younging pattern towards the rim (Fig. 7b).

5.5. *Sample HP-34C (Western peripheral pluton)*

Four grains were mapped: *M1* ($N = 85$), *M3* ($N = 72$), *M4* ($N = 85$) and *M5* ($N = 145$), all yielding significantly older ages than grains in the other locations, between 1.45−2.00 Ga (Fig. 8). All PDD and IAF spectra show a broad unimodal peak centered about 1.65−1.70 Ga. The PDD curve for grain *M4* appears smoother due to larger errors in individual ages. Unlike the central pluton samples, the age maps do not show a well-defined geometric pattern but instead multiple peaks and troughs of older and younger ages scattered throughout the crystals. Despite these much older ages, the youngest ages are all located on the rims.

6. MUSCOVITE CHEMISTRY AND MICROSTRUCTURE

To check for compositional correlations with internal $^{40}Ar/^{39}Ar$ variations, extensive microchemical analyzes were carried out on individual crystals and across multiple crystals in three critical samples, HP-10D, HP-13A, and HP-34C. Electron microprobe analyses show that muscovite crystals from the central pluton (HP-10D and HP-13A) have broadly the same chemical composition (Table 2, Fig. 9), with slight inter-facies variations notably illustrated by the higher Mg content of HP-10D muscovite (Fig. 9b). Muscovite in the western peripheral facies HP-34C is distinctly enriched in Si but has lower Fe contents than the central facies (Fig. 9a,b). Significantly, and despite these differences, all samples show a systematic K ↔ Na anti-correlation (Fig. 9c). EMP compositional profiles performed along (001) in two muscovite grains (one from HP-13A, the other from HP-34C) reveal that the anti-correlation K ↔ Na is spatially associated to a rim-ward decrease in Na concentration and a concomitant increase in K (Fig. 10). Though less pronounced, a Fe ↔ Mg anti-correlation is also apparent along these profiles with an increase in Fe towards the rims (more apparent in the HP-13A grain) and a concomitant decrease in Mg (more visible in the HP-34C grain). The Si content appears homogeneous in both samples. The Al content is homogeneous in muscovite HP-13A and increases slightly towards a rim in muscovite HP-34C (Fig. 10b).

For context with *in situ* $^{40}Ar/^{39}Ar$ variations, SEM maps were performed on the $^{40}Ar/^{39}Ar$ mapped split #1 and #2 of *M19* from HP-13A and split #1 from HP-13A *M21* (Fig. 11, **Supplementary Material B**). As with the EMP data, while no dominant pattern is observed for all major elements, Na and K display a marked anti-correlation with a systematic

Na decrease towards the rims, locally observed also inside the crystals. The target-matching approach employed to correlate isotope patterns with elemental patterns reveals that these antithetical variations are strongly coupled to the apparent $^{40}Ar/^{39}Ar$ variations along (001). The slight but significant contrast in Na content from EDS maps unambiguously correlates with the $^{40}Ar/^{39}Ar$ patterns (compare in particular Fig. 11c with Fig. 6f). The correlation is even more apparent in selected profiles showing sympathetic variations in Na content and apparent $^{40}Ar/^{39}Ar$ age (Fig. 11). The zones depleted in Na correspond to apparent younger ages, and vice versa.

STEM characterization was carried out to further refine the compositional−isotope correlations in connection with crystal microstructure. Microstructural investigations were performed on two grains of HP-13A (Split #2 of *M19*, Split #2 of *M21*), as well as on grain *M11* of HP-10D (not chemically analyzed). FIB foils were extracted to compare areas depleted in Na and corresponding to younger ages, with areas enriched in Na preserving older ages (Fig. 12). In all foils, STEM images reveal the presence of extended defects parallel to the basal plane and distributed across the crystals (Fig. 12a-c). However, the density of these defects differs drastically between zones differing in Na content. Microstructural defects are much more abundant in Na-depleted zones with younger ages than in Na-rich areas preserving older ages. High magnification TEM imaging of a FIB foil extracted from a Na-depleted area of the grain HP-10D (*M11*) reveals the defects to be (001)−parallel lenticular delaminations 10 to a few hundred nm-long and up to 10 nm-wide (Fig. 12d).

7. DISCUSSION

7.1. Significance of the $^{40}Ar/^{39}Ar$ gradients

The intracrystalline concentric age pattern revealed for all HPG micas is consistent with previous $^{40}Ar/^{39}Ar$ crystal-mapping studies of igneous micas that suggest intra-crystalline ^{40}Ar transport driven by diffusion along (001) with a strong control of grain boundaries and internal microstructural defects (Phillips and Onstott, 1988; Onstott et al., 1991; Phillips, 1991; Hames and Hodges, 1993; Hodges et al., 1994; Hodges and Bowring, 1995). Noteworthy, all micas in the HPG concentrate the youngest ages near the rims around a common value near 1.30−1.35 Ga. The only exceptions are the grains from the peripheral sample HP-34C.

On the other hand, all grains retain one (or more) irregular "core" zone(s) with variably older ages, from 1.60 Ga up to 1.73 Ga (again excluding HP-34C). Importantly, the oldest recorded ages (1.73 ± 0.03 Ga, excluding HP-34C) are strikingly close to the intrusion age estimated between 1.70 to 1.73 Ga (cf. section 2). Accordingly, we see these ages as geologically meaningful and closely matching, within the resolution of individual $^{40}Ar/^{39}Ar$ spot ages (± 30 Ma, 1σ), early (magmatic) HPG growth by stepwise coalescence of multiple sills (Nabelek et al., 2010).

Standing apart are the older ages recorded by muscovite in HP-34C (western peripheral pluton). These ages suggest muscovite growth from a melt initially enriched in ^{40}Ar, with wholesale incorporation of large amounts of non-radiogenic ^{40}Ar during or after crystallization. The fact that the youngest ages are found at the rims argues for the first hypothesis, implying subsequent diffusive re-equilibration of the initial excess (Fig. 8). The much older ages of this sample compared to the others from the central pluton are also paralleled by a distinctly higher Si content (Fig. 9a), suggesting particular compositional-genetic relationships specific to that peripheral pegmatitic facies.

The collective preservation (except for HP-34C) of near-intrusion "core" ages surrounded by an outward, diffusive-like, younging pattern is consistent with protracted cooling from initial (magmatic) stages followed by regional (crustal) slow cooling over hundreds of Myr, as previously inferred from regional-scale concentric biotite + muscovite $^{40}Ar/^{39}Ar$ ages mapped across the HPG metamorphic aureole (Dahl and Foland, 2008). Note that the regional $^{40}Ar/^{39}Ar$ pattern excludes diffusive reopening by a later reheating pulse to explain the common "rim" age at ca. 1.30 Ga in HPG muscovite (see above). Partial diffusive resetting is not supported either by the lack of any recognized thermal event of this age in the area (Dahl and Foland, 2008).

In situ closure $^{40}Ar/^{39}Ar$ gradients of such an extent have been already documented in igneous micas from other slowly-cooled intrusives elsewhere in the southwestern United States Proterozoic orogenic belt (south-central Arizona: Crazy Basin monzogranite, Hames and Bowring, 1994; Hodges et al., 1994; Horse Mountain biotite, Hodges and Bowring, 1995). Such internal age gradients due to slow cooling were not anticipated here on account of the dominantly flat $^{40}Ar/^{39}Ar$ release spectra previously documented by step-heating experiments

on HPG muscovite (Dahl and Foland, 2008; Holm et al., 1997). As emphasized by Hodges and Bowring (1995), incremental heating results in dehydroxylation of micas that can homogenize intracrystalline ^{40}Ar gradients, as independently shown by Gaber et al. (1988) and Sletten et al. (1998). Such an artifact is also demonstrated by our new data and most likely explains why this feature passed undetected in past ^{40}Ar/^{39}Ar studies of the HPG and its country rocks.

7.2. ^{40}Ar diffusion-domain structure of HPG muscovite

The irregular geometry of the age gradients along (001) in all HPG muscovite grains indicates that ^{40}Ar retention during progressive cooling was not strictly controlled by a single volume-diffusion mechanism. This pattern is reminiscent of the complex ^{40}Ar/^{39}Ar closure gradients just mentioned for the slowly-cooled micas analyzed by Hames and Hodges (1993), Hodges et al. (1994), and Hodges and Bowring (1995). This pattern was explained by Hodges and Bowring (1995) via a double mechanism involving volume diffusion on a scale comparable to that of the grain radius with rapid diffusion along discrete zones of high crystal defect density. Subsequent work by the Lausanne group (notably Kramar et al., 2001, 2003; Kramar, 2002) indeed showed that internal deformation structures can promote localized intracrystalline ^{40}Ar loss in strongly deformed (porphyroclatic) muscovite via a network of localized defects (unit dislocations and stacking faults bordered with partial dislocations) cutting across the crystal. The Crazy Basin and Horse Mountain monzogranites cooled mostly underformed after static crystallization (as the HPG did), which excludes subsolidus deformation as a major cause for defect-enhanced ^{40}Ar loss in these texturally simple micas. Unfortunately, neither Hames and Hodges (1993), Hames and Bowring (1994), Hodges et al. (1994), nor Hodges and Bowring (1995) could document the intracrystalline structure of their samples to aid in the identification of the microstructures responsible for the irregular domain-like ^{40}Ar loss pattern produced during progressive cooling.

Here, the combination of high spatially-resolved *in situ* ^{40}Ar/^{39}Ar dating, microchemistry, and high-resolution electron microscopy data unambiguously document direct coupling between age, composition and microstructure. In particular, our data show that the ^{40}Ar/^{39}Ar gradients and Na/K variations are coupled at the scale of the whole grains, to the point

of permitting targeting of critical zones for TEM imaging based on the observed isotope-elemental patterns. This allows us to address fundamental aspects of the diffusion-domain structure of muscovite, notably (*i*) the origin of the observed Na/K zoning, (*ii*) the relationship to microstructural defects, and (*iii*) their respective role in the development of the ^{40}Ar diffusional gradients. These aspects are explored in turn below.

7.2.1. Origin of K ↔ Na zonations

The dependence of ^{40}Ar diffusion on the Na/K ratio is obvious from the close spatial association between domains featuring younger ages and low Na/K ratios, mostly around the rims but also invading the grain interiors (Section 6). Less apparent is the nature of the interaction coupling elemental with isotopic transfer at the scale of the whole crystals and the interlayer proper.

The textural Na/K pattern is systematic, both within grains of the same sample and across the sample suite as a whole. Atomic K ↔ Na interdiffusion is attested by the near-unity ratio between the number of atoms lost (Na) to those gained (K) in muscovite from HP-13A and HP-34C (Fig. 13). Texturally, the Na and K concentration profiles near the muscovite rims are smooth and distinct from stepped profiles typically associated with overgrowth (Sio et al., 2013). This implies K ↔ Na substitutional exchange (sometimes paralleled by a sympathetic Fe ↔ Mg substitution as well) due to grain-boundary disequilibrium independent of bulk composition and driven by post-crystallization interaction with either some K-rich residual magmatic liquid near the solidus (or any exsolved fluid from the magma), or late K-rich hydrothermal fluids after complete solidification.

Disequilibrium interactions with intercumulus residual liquid at near-solidus temperatures can result either in topotactic overgrowth by a chemically distinct rim, or in crystal dissolution with replacement by other phases. Petrographic observations show that some muscovite grains are corroded/embayed and locally replaced by magmatic phases (e.g., quartz; Fig. 2e, f), effectively indicating local/transient disequilibrium with the residual melt. EMPA traverses show that local Na/K gradients are not truncated by partial dissolution-replacement textures, and thus post-date (or accompany) resorption at magmatic-T (Fig. 10b). A high-K residual melt was invoked by Nabelek and Ternes (1997) to explain the chemical and textural

relationships between aplitic and pegmatitic layers in the HPG. They suggest magma evolution characterized by liquidus crystallization of sodic minerals (plagioclase and tourmaline) under low H_2O activity, followed by crystallization of a relatively potassic residual melt under higher H_2O activity. Oxygen isotope ratios between quartz and other minerals indicate $\Delta^{18}O$ equilibration values between 800 and 650 °C, between liquidus and solidus (Nabelek et al., 1992b). δD values in micas are also compatible with magmatic temperatures, except for limited post-crystallization interactions with non-magmatic fluids in the southern part of the HPG (Nabelek et al., 1992b). Coupled with the resorption texture, these high-T estimates are consistent with incongruent dissolution coeval with partial re-equilibration of muscovite to higher Na/K values at the rims locally affected by replacement (and locally reaching into the core as well, Fig. 10b).

Fluid-inclusion microthermometry of HPG quartz and tourmaline provides evidence for two generations of magmatic fluids trapped in at least three types of inclusions (Nabelek and Ternes, 1997; Sirbescu and Nabelek, 2003). Type 1 inclusions are H_2O + CO_2 mixtures trapped as primary inclusions at temperatures above the solidus in magmatic quartz and tourmaline. Type 2 and 3 inclusions are secondary inclusions trapped along healed microfractures in quartz. These are rich in H_2O and CO_2, respectively, and are interpreted to have resulted from re-equilibration and unmixing of Type 1 fluids that progressively changed composition and density with decreasing temperature and pressure. They were trapped under subsolidus conditions and are likely candidates for late-stage interaction and exchange with muscovite at subsolidus conditions as well. While the low solubility of alkali chlorides in CO_2-rich fluids (Webster et al., 1989) precludes the carbonic fraction from causing K enrichment, the abundance of alkalis (including Na, K, and Li) is noted in primary mixed fluid inclusions (Nabelek and Ternes, 1997; Sirbescu and Nabelek, 2003). $(Na/K)_{musc}/(Na/K)_{fluid}$ exchange partitioning strongly favors incorporation of K over Na into muscovite, even at low Na/K fluid-ratios (Volfinger 1976). This may explain the inward K enrichment seen in muscovite, although this is not texturally tied to the muscovite habitus as is the resorption at magmatic temperatures. K-rich aqueous fluids coupled to textural replacement are documented only locally in the contact aureole, but in the reverse sense with staurolite replaced by muscovite (Nabelek et al., 2006).

Together, textural, fluid-inclusion thermometry, and stable isotopes relationships argue for Na/K interchange occurring either at late-magmatic or subsolidus conditions, in any case very early during high-T cooling + solidification of the HPG. Kinetically, the nature of the interaction between K $\leftrightarrow$ Na interdiffusion and ^{40}Ar diffusion is unlikely to have involved dynamic coupling. The inward K $\leftrightarrow$ Na diffusion profiles are on average 300 μm−long (Fig. 10 and Fig. 11). Considering a diffusion coefficient for K of 6×10^{-17} cm^2.s^{-1} at 650 °C (Nteme et al., 2022), a diffusion duration of only $\sim$ 0.1 Myr is required to produce such profiles. This is more than three orders of magnitude shorter than the time span of several hundreds of Myr recorded by the ^{40}Ar/^{39}Ar zoning patterns. These timescales are clearly decoupled and indicate that solid-state K $\leftrightarrow$ Na interdiffusion must have stopped well before the development of intracrystalline ^{40}Ar/^{39}Ar age gradients.

7.2.2. Genetic connection to lenticular defects

While direct (dynamic) coupling cannot be invoked between ^{40}Ar diffusion and K $\leftrightarrow$ Na exchange, static-compositional effects can indirectly affect ^{40}Ar diffusivity via the modifications they impart to the mica structure, notably via the $FeMg_{-1}$ substitution and Tschermak exchange (e.g., Norwood, 1974; Harrison et al., 1985; Scaillet et al., 1992; Dahl, 1996). K $\leftrightarrow$ Na substitution along the muscovite-paragonite join similarly involves crystallographic modifications, in particular the decrease of the interlayer spacing along the c−axis with increasing Na (Guidotti, 1984). This may increase the migration barrier for ^{40}Ar along the (001) plane, potentially lowering diffusivity in Na-rich domains. However, the overwhelming abundance of the interlayer cation K ($\sim$ 0.90 a.p.f.u) over Na ($\sim$ 0.07 a.p.f.u) and the relatively modest change in K/(K+Na) ratio between Na-rich and Na-poor zones ($<$ 1 %) in HPG muscovite are unlikely to have induced major variations in effective ^{40}Ar diffusivity across compositionally distinct zones. This is independently corroborated by Molecular Dynamics simulations as well (Nteme, 2021).

Coupled variations between ^{40}Ar/^{39}Ar age and Na/K ratio have been already documented by Boundy et al. (1997) in muscovite from eclogites of the Holsnøy Island (Norway). Using target-matching techniques as here, they found homogeneous *in situ* laser ages around 443 Ma in crystals with homogeneous Na/K ratio, in contrast to much older and heterogeneous

ages (445−625 Ma) in muscovite exhibiting higher and variable Na/K. Resolved (5−100 nm scale) analytical electron microscopy (AEM) on the same sample revealed variable Na/K, but no separate paragonite domains. In contrast, muscovite grains with homogeneous ages showed little Na/K variability at the microprobe level. A broad, within-crystal, correlation was suggested between Na-rich zones and older ages inside their sample BA59/89 (grain 1), but the cross-matching coverage is less well-resolved than here. This precluded clear attribution of compositional effects on internal $^{40}Ar/^{39}Ar$ patterns. Although no discernible intracrystalline defects were detected, splitting of SAED ($00l$) diffraction patterns indicated intergrown micas with different basal spacing, most probably muscovite and sodic muscovite interlayered at the unit cell level (< 5 nm). To explain the irregular ^{40}Ar distribution, Boundy et al. (1997) invoked a process of volume-diffusive loss of excess ^{40}Ar initially incorporated at eclogite-facies conditions, locally mediated by nanostructural heterogeneities at the scale of the interlayer.

In our case, layer-parallel defects (lenticular voids and basal parting) are seen that directly correlate in distribution and density with the Na/K maps (and the $^{40}Ar/^{39}Ar$ ages). Identification of these nanostructures and their interpretation as primary defects is not unequivocal however. Lenticular voids parallel to (001) similar to those documented are reported in other TEM studies of phyllosilicates (Veblen, 1983; Ahn et al., 1986; Amouric, 1987; Goodwin and Wenk, 1990; Merriman et al., 1990; Onstott et al., 1991; Phillips, 1991; Shau et al., 1991; Ahn and Buseck, 1998; Giorgetti et al., 2000; Kramar, 2002; Capitani et al., 2016; Aslin et al., 2019). They have been variably attributed to Guinier-Preston zones (Onstott et al., 1991; Phillips, 1991), deformation (Amouric, 1987; Kramar, 2002; Aslin et al., 2019), or electron beam damage (Veblen, 1983; Ahn et al., 1986; Goodwin and Wenk, 1990; Merriman et al., 1990; Shau et al., 1991; Ahn and Buseck, 1998; Giorgetti et al., 2000; Capitani et al., 2016).

By exposing paragonite to increasing durations and intensities of TEM electron beam, Ahn et al. (1986) observed a progressive degradation of the crystal structure manifested by abundant delaminations (lenticular voids) normal to the $c-$axis. These were correlated to a loss of Na leaving Al and Si unaffected. The voids were interpreted as damage zones caused by Na loss from the interlayer region under the beam, with the collapse of the paragonite structure to a pyrophillite-like structure causing volume loss and reduction of basal spacing.

Mechanical parting of paragonite layers along (001) was inferred to be caused by the release of the elastic strain due to local collapse of the structure.

Our FIB samples were imaged by STEM at 30 kV. To investigate the effect of extended exposure to the beam, a succession of three images was gathered over the same area of a FIB foil from grain *M11* of HP-10D but the defects observed in the first image did not evolve appreciably further on (see **Supplementary material C**, Fig. S-C-1). Further FIB testing of another muscovite with similar composition under identical thinning and beam conditions revealed no visible microstructural defect (muscovite SSY92-9, St. Sylvestre leucogranite, Massif Central, France; Scaillet et al., 1996) (**Supplementary material C**, Fig. S-C-2). Together, both tests rule out beam and thinning artifacts as the primary cause of the observed defects as they would have equally affected both specimens. Note also that lenticular voids commonly identified as beam damage in white micas are systematically reported for Na-rich (paragonite) endmembers (Ahn et al., 1986; Giorgetti et al., 2000), not for compositionally intermediate micas with low Na/K as studied here (and in Boundy et al., 1997, who could not identify beam damage in their moderately Na-enriched muscovite either).

These observations strongly argue for the defects being primary. Because the muscovite samples are undeformed, the critical observation that the density and distribution of defects correlate with the intracrystalline Na/K zoning (Fig. 12) suggests a genetic link with the K $\leftrightarrow$ Na exchange during early (near-solidus) cooling as discussed in Section 7.2.1. Microstructural defects induced by K $\leftrightarrow$ Na interdiffusion have not been described as such in micas, but are known in alkali feldspar (Neusser et al., 2012; Scheidl et al., 2014; Petrishcheva et al. 2019). In feldspar, lattice mismatch between Na- and K-rich domains produced by local variations in K $\leftrightarrow$ Na exchange can result in tensile stress buildup triggering internal fracturing once a threshold is exceeded (Scheidl et al., 2014). In micas, K and Na segregate along the interlayer plane into immiscible nanodomains of pure muscovite and paragonite due to their different sizes (Shau et al., 1991; Livi et al., 2008). The segregation of interlayer cations into immiscible nanodomains is coupled with the segregation of octahedral cations as well (Livi et al., 2008), so that paragonite domains have higher Al/Si ratio than muscovite domains (which are more phengitic). Such coupled changes involve rotation and corrugation of the tetrahedra required to match the smaller Na into the XII site while the octahedra become

larger and tend to flatten with increasing phengite content. At some point, the tetrahedral and octahedral sheets can no longer fit together (Radoslovich, 1960; Guidotti, 1984) and the stress buildup due to the mismatch at the interface between the muscovite and paragonite nanodomains may trigger splitting along the interlayer, producing the observed lenticular defects.

To conclude, the higher defect density seen in K-substituted, Na/K intermixed, subdomains of HPG muscovite may be either a direct manifestation of incoherent stress-induced delamination nucleating between isostructural packets of layers with variable Na/K ratio (Fig. 12), or the indirect consequence of structural recombination due to Na−K segregation at the elementary stacking level (nanodomains). Along with the Holsnøy precedent (Boundy et al., 1997), these observations suggest that K ↔ Na exchange materially affects the interlayer ^{40}Ar diffusivity of white micas. The irregularly depressed non-Fickian profiles seen near the rims and locally reaching into the core indicate that ^{40}Ar diffusivity is enhanced directly by these microstructural defects or via the underlying substitutional-structural mechanism(s) affecting the interlayer. This further suggests that these defects, although appearing isolated, must be interconnected into a network of pathways to provide access to the external grain-boundary medium. They do not necessarily act as traps as sometimes suggested (e.g. Camacho et al., 2012). Importantly, inter-split variations in K ↔ Na exchange (Fig. 11 and Fig. 12) and ^{40}Ar/^{39}Ar maps (Fig. 6c,d,e,f) show that these channeled, layer-parallel, defects involve little cross-layer communication beyond 50 μm (the penetration depth of the UV−probe).

7.3. ^{40}Ar diffusion geometry and multipath diffusion

Depending on their topology (e.g., crystallographic orientation, spacing, distribution, and interconnectivity), extended lattice defects can either impart a discrete multi-domain diffusion behavior (MDD model, Lovera et al., 1989), or a wholesale multi-path diffusion regime where two or more mechanisms continuously interact through the bulk of the crystal (Phillips, 1991; Lee, 1995). Schematically, the MDD model assumes no interaction between sub-crystal domains with instant (very-high diffusivity) access to the grain boundary network whenever a domain boundary is reached. In contrast, the multipath model assumes a continuum across the lattice till the grain boundary.

The mapped $^{40}Ar/^{39}Ar$ distributions bear directly on such "continuous *vs.* discrete" typology of the diffusive network along (001). Rather than the juxtaposition of discrete sub-domains, the internal age contours and gradients interpolated by kriging reveal a dominantly fuzzy pattern with a diffusive lengthscale commensurate with the grain size (Figs. 5, 6, 7). The extent of the age gradients clearly indicates that the interpolated $^{40}Ar/^{39}Ar$ scalar fields are a fair representation of the true ^{40}Ar intragrain diffusive network. In parallel, optical and electron microscopy reveal an array of layer-parallel nano-structural defects disseminated and correlated to the K $\leftrightarrow$ Na exchange at the scale of the whole crystals (Section 7.2.2), with no evidence of intragranular cracks, kinks, or segmentation susceptible to cut across (and reduce) the effective diffusion radius.

We tested the continuous *vs.* discrete ^{40}Ar diffusion-domain typology by plotting the apparent percentage of defect-rich areas integrated along (001) against the maximum age recorded by grains of the central pluton (including pits only distributed over the same topmost surface layer). The percentage of defect-rich areas cannot be assessed directly but may be approximated by the areal proportion of zones featuring apparent ages younger than 1.5 Ga. This threshold is arbitrary but corresponds to the isopleths in the $^{40}Ar/^{39}Ar$ maps that most closely match the zones of coupled Na-defect pattern in Fig. 11 and Fig. 12. The plot (Fig. 14a) reveals a well-defined negative correlation for a collection of grains varying widely in shape and average radius (note that the correlation remains fairly identical, $R^2 > 0.8$, for a cut-off between 1.43−1.59 Ga). The internal age variability does not correlate in any obvious way with the average radius of the crystals (Fig. 14b). In particular, we see no scaled progression between the maximum age(s) recorded in a crystal and the shortest distance to the rim or a discrete fast-path drain or grain segmentation hypothetically running nearby (i.e., the MDD prediction; Fig. 14c). Instead, the negative correlation indicates that, at any point in the muscovite crystals and irrespective of their dimension, the oldest recorded age is directly controlled by the overall defect structure integrated throughout the whole grain, not by discrete extended defects located nearby. This observation strongly argues for the multipath model and flies in the face of the notion that MDD modeling of muscovite incremental heating data is an adequate description of the processes taking place in real samples.

A multipath model accounting for the presence of layer-parallel defects was already suggested for muscovite by Kramar and co-workers (Kramar et al., 2001, 2003) to explain preferential ^{40}Ar loss along stacking faults developed along (001) by basal slip during intragranular shear. Basal slip by partial dislocation glide along (001) leads to localized repulsive forces with a net dilation (and enhanced ^{40}Ar mobility) along the interlayer. While transient, the transport efficiency along these defects can be much greater than pipe diffusion because the volume fraction of the lattice swept over by moving dislocations during ongoing deformation is orders of magnitude higher (Kramar et al., 2003). In the HPG case there is clearly no such a deformation drive. This role is played by the irreversible modifications brought about by the K $\leftrightarrow$ Na exchange that locally served as a guide for enhanced ^{40}Ar diffusion along (001).

Summing up, the spatial continuum inferred from the ^{40}Ar concentration gradients calls for a model combining multi-path diffusion with spatially variable domains characterized by distinct bulk diffusivities. These are internally controlled by their own defect density leading to a mosaic of high-diffusivity *zones* (rather than *pathways*) coexisting with (or transitioning smoothly into) low-defect zones preserving near-regular lattice diffusion constants.

7.4. Quantitative modeling of the ^{40}Ar diffusion-domain structure

To contrast quantitatively the diffusion rates in defect-poor (slow-diffusing) domains with those prevailing in defect-rich (fast-diffusing) domains, we devise a simple 2D diffusion model along (001) according to:

$$\frac{\partial C}{\partial t} = D(t)\left(\frac{\partial^2 C}{\partial x^2} + \frac{\partial^2 C}{\partial y^2}\right) + S(t) \tag{1}$$

where C is the ^{40}Ar concentration, $D(t)$ its time-varying diffusivity, and $S(t)$ the production term due to spontaneous ^{40}K decay:

$$S(t) = \lambda_e \, {}^{40}\mathrm{K}_0 \exp(-\lambda t) \tag{2}$$

with $\lambda_e = 0.581 \times 10^{-1}$ Ga^{-1} and $\lambda = 5.543 \times 10^{-1}$ Ga^{-1} (Steiger and Jäger, 1977). $^{40}\mathrm{K}_0$ is the initial K concentration at t_0. We consider a cooling model deduced from independent $T-t$ couples reviewed in Dahl and Foland (2008) and parametrized as (cf. Fig. 15):

$$T_{\mathrm{mid}}(t) = 272 \exp(-0.04t) - 0.409t + 751 \tag{3}$$

with T_{mid} in Kelvin and t in Ga. The exponential term accounts for conductive cooling *in situ* in the country rocks, followed by steady-state (linear) cooling of the crust (+ intrusion) during progressive exhumation (see discussion in Dahl and Foland, 2008). Bounding curves $T_{\mathrm{min}}(t)$ and $T_{\mathrm{max}}(t)$ are defined to bracket the cooling curve arbitrarily within ± 50 °C (Dahl and Foland, 2008). Homogeneous initial and boundary conditions are assumed at $t_0 = 1.715$ Ga, along with spatially uniform $^{40}\mathrm{K}_0$ and $S(t)$ across all crystals during cooling. Since the HPG was emplaced at shallow depths with protracted cooling during tectonic quiescence (very slow exhumation; Holm et al., 1997; cf. Section 2), the pressure effect on $D(t)$ is neglected in the model. The loss-production Eq. (1) is solved by a finite-element scheme accounting for the specific grain geometry in 2D along (001) under MATLAB®. The computed 2D ^{40}Ar concentration field is converted into a map of apparent ages, t_{app}, via:

$$t_{\mathrm{app}} = \frac{1}{\lambda} \ln \left(1 + \frac{\lambda}{\lambda_e} \frac{C(t)}{\mathrm{K}(t)} \right) \tag{4}$$

where $C(t)$ and $K(t)$ are the concentration of ^{40}Ar and ^{40}K at time t, respectively.

7.4.1. Defect-free ^{40}Ar diffusion kinetics

Our goal here is to model ^{40}Ar volume diffusion in grains that preserve regular concentric gradients with core values approaching or overlapping the HPG intrusion age (≥ 1.70 Ga). This age is found in four grains from the central pluton (HP-10D (*M9*), HP-10D (*M10*), HP-10D (*M11*) and HP-13A (*M21*-#1), Fig. 5 and Fig. 6e), indicating that diffusive loss out from the core of these grains became inefficient very early during subsolidus cooling. An estimate of the maximum diffusivity preserving these core ages would provide an upper empirical bound on ^{40}Ar diffusivity.

We focused on muscovite *M11* of HP-10D (Fig. 5d). In addition to exhibiting regular concentric age gradients centered on an intrusion-like age of 1.73 ± 0.03 Ga, this grain retains original pristine edges with dimensions representative of most other grains. Assuming a spatially homogeneous volume-diffusion coefficient D_{v} given by:

$$D_{\mathrm{v}}(t) = D_0^{\mathrm{v}} \exp \left(- \frac{E_{\mathrm{v}}}{RT(t)} \right) \tag{5}$$

we use Eq. (1) along with the cooling models of Fig. 15 to find the maximum frequency factor D_0^{v} reproducing the core age for a range of exploratory activation energies typical of micas

(including biotite and phlogopite: $E_v = 40-70$ kcal.mol^{-1}; Robbins, 1972; Giletti, 1974; Harrison et al., 1985; Hames and Bowring, 1994; Grove and Harrison, 1996; Kirschner et al., 1996; Harrison et al., 2009; Forster and Lister, 2014; Nteme et al., 2022). The $E_v-D_0^v$ pairs empirically found to fit the core retention age trade-off in Arrhenian space with a single well-defined cross-over point for each model considered (Table 3). In an Arrhenius plot (Fig. 16a), these collectively define a diffusivity domain (orange field) delineating an upper bound below which any $E_v-D_0^v$ couple would preserve the core age as well. Experimental and empirical diffusion estimates (Hames and Bowring, 1994; Kirschner et al., 1996; Harrison et al., 2009) plot up to two orders of magnitude above this upper bound. In contrast, the Arrhenian relationship derived from atomistic simulations by Nteme et al. (2022) plots within the domain, independently supporting the sluggish ^{40}Ar diffusion behavior theoretically predicted for undefective muscovite. Remarkably, while reproducing the target core age, the modeled $E_v-D_0^v$ pairs all predict a rather flat core-to-rim profile, at odds with the depressed gradients empirically revealed by ^{40}Ar/^{39}Ar crystal-mapping (Fig. 16b). Such a mismatch clearly indicates that the observed age distribution should be approximated with a composite model allowing for substantially higher diffusion rates than those preserving the core age.

7.4.2. Defect-enhanced ^{40}Ar diffusion rates

We now test a spatially-variable diffusion model in which ^{40}Ar migrates simultaneously along defect-poor and defect-rich paths with different diffusivities. This case has been already treated by Kramar et al. (2003) to account for extended intracrystalline defects affecting the internal diffusion-domain structure of deformed porphyroclastic muscovite in a mylonite. The diffusion coefficient in Eq. (1) is replaced by an effective diffusion coefficient defined as (Hart, 1957):

$$D_{\text{eff}}(t) = f_d D_d(t) + (1 - f_d) D_v(t) \tag{6}$$

where f_d is the volume fraction of defects in the considered domain and D_d the limiting diffusivity along the defective path. Eq. (6) provides an upper limit for D_{eff} in the case of diffusivity along parallel pathways, which amounts to neglect tortuosity. The defect density (here f_d) is assumed to be low on account of STEM observations. On the other hand, the contrast between D_v and D_d should be high to allow strongly depressed ^{40}Ar/^{39}Ar gradients

to develop away from the cores (Fig. 16b). In the limit $f_d \ll 1$ and $D_v \ll D_d$, Eq. (6) simplifies to its first term that we assume to follow the Arrhenian form:

$$D_{\text{eff}}(t) = f_d D_d(t) = f_d D_0^d \exp\left(-\frac{E_d}{RT(t)}\right) \quad (7)$$

A mean-field approximation making no assumption of specific diffusive anisotropy (the Maxwell approximation) would reduce this estimate by a factor of 2/3 (Mehrer, 2007), which is immaterial in terms of order-of-magnitude characterization of the process. ^{40}Ar diffusivity in microstructural defects is poorly constrained, but an activation energy between 40−45 kcal.mol^{-1} is commonly assumed (Lee, 1993; Kramar, 2002). In the following, we take E_d = 45 kcal.mol^{-1}.

We focused again on muscovite *M11* of HP-10D, including also the splits of grains *M21* and *M19* from HP-13A (Fig. 5d and Fig. 6c,d,f). The crystals were subdivided into several sub-grain domains mimicking the Na/K and/or age zoning and the lumped parameter $\psi_d = f_d D_0^d$ was then adjusted by trial and error for each domain to match the internal 2D age pattern. Best-matching ψ_d values adjusted for each domain in each grain are listed in Table 4. The geometry and extent of the modeled domains are displayed for each grain in Fig. 17 along with the empirical ^{40}Ar/^{39}Ar age map, the simulated age map, and a selected profile comparing observations with predictions. For a fair comparison, the simulation maps were interpolated via Surfer® 13 based on the nodes strictly coinciding with the *in situ* position of the ablation pits across the crystals. Fig. 17 shows that the 2D ^{40}Ar/^{39}Ar grain-scale patterns are fairly well reproduced by this relatively simple model. Core-to-rim ^{40}Ar/^{39}Ar age profiles broadly agree between observations and model, although in some cases the oldest age is not well reproduced (e.g., *M11* grain of HP-10D, Fig. 17a).

Diffusivity estimates empirically inferred for defect-rich sub-domains in the four modeled grains define a broad domain in Arrhenian space (blue field in Fig. 18). These are enhanced by a factor of up to 6 or 10 orders of magnitude (between 700−300 °C) compared to the ideal, defect-free, lattice diffusion model (Nteme et al., 2022, trend labelled "4" in Fig. 18). This enhancement accounts for an overall "extra" loss around 15 % as estimated from the mean age of each individual muscovite grain relative to the intrusion age (1.715 Ga). Along with previous studies (Kramar et al., 2001, 2003), these results show that microstructural

defects can considerably affect ^{40}Ar retention properties of muscovite, including undeformed primary magmatic specimens. Interestingly, all previous experimental and empirical diffusion estimates (Hames and Bowring, 1994; Kirschner et al., 1996; Harrison et al., 2009) plot within the domain of enhanced diffusivity defined in Fig. 18, suggesting they likely derive from muscovite containing microstructural defects as well. Combined with theoretical predictions (Nteme et al., 2022) and the present results, these field and laboratory-based estimates collectively define the $D-T$ field probably spanned by ^{40}Ar kinetics in natural muscovite (dashed domain in Fig. 18).

Implicit in Eq. (7) is that the limiting diffusivity $D_{\rm d}(t)$ is the same for all defective domains, and that the inferred variations in ψ_d (Fig. 17 and Table 4) directly correlate to spatial variations in $f_{\rm d}$ (and the implied orders-of-magnitude variations in relative defect densities). If, as is more likely, $f_{\rm d}$ and $D_0^{\rm d}$ are not directly (linearly) coupled, ψ_d variations cannot be tied to defect density variations. This is the main issue still to be resolved. Further characterization by dedicated FIB-STEM/TEM imaging and MD modeling is clearly required to understand how $D_0^{\rm d}$ and $f_{\rm d}$ are coupled in terms of defect structure and enhanced atomic-scale ^{40}Ar mobility.

8. SUMMARY AND CONCLUSIONS

^{40}Ar diffusion in slowly cooled muscovite from the HPG pluton has been investigated using target-matching techniques combining extensive ^{40}Ar/^{39}Ar *in situ* mapping ($>$ 1,600 individual measurements) with elemental mapping and high resolution electron microscopy. The main results can be summarized as follows.

- ^{40}Ar/^{39}Ar crystal-mapping reveals irregular, mm-size, concentric age patterns due to protracted cooling across the ^{40}Ar retention interval of muscovite; these define a mosaic-like structure with sub-domains, broadly $\sim 250-300$ μm across, separated by zones of high diffusivity varying in shape and extent along (001).

- Each grain is unique, with splits of the same crystal recording themselves widely varying internal ^{40}Ar/^{39}Ar patterns and extent of retentivity. The maximum ages preserved in

the core(s) are unrelated to either the size of the specific subdomain or the overall dimension of the host crystal; they vary primarily in connection with the areal extent of high-diffusivity zones distributed all over (001) across the micas. Inter-split variations in ^{40}Ar diffusion pattern indicate strong diffusion anisotropy with little communication (if at all) across the interlayer beyond 50 μm (the penetration depth of the UV−probe).

• A striking spatial association is documented between sub-domains with younger ages, low Na/K ratios, and high density of microstructural defects (basal parting) seen through FIB-STEM/TEM. These defects are argued to have formed in response to inward K $\leftrightarrow$ Na interdiffusion during late magmatic stages and prior to protracted crustal cooling. The diffusion-domain structure of HPG muscovite thus appears passively controlled by elemental substitutions and their consequences at the level of the interlayer in terms of structural stability and chemical reactivity.

• The diffusion-domain structure along (001) in white micas is documented as a spatial continuum at the scale of the whole grains down to the UV−probe lateral resolution ($\sim$ 35 μm). Grain-scale internal ^{40}Ar/^{39}Ar diffusion gradients cannot be reproduced with 2D Fickian-type profiles assuming homogeneous diffusion under protracted cooling. The mechanism invoked is one of continuous grain-scale interactions between subdomains with different diffusivity along (001), and is fundamentally distinct from domain-like segmentation produced by discrete high-diffusivity linear or planar defects cutting across the cleavage plane.

• Quantitative modeling shows that ^{40}Ar diffusivity through defect-poor subdomains is very sluggish, at least two orders of magnitude lower than existing experimental and empirical estimates, but consistent with Molecular Dynamics estimates for undefective muscovite (Nteme et al., 2022). In contrast, defect-rich domains are characterized by ^{40}Ar diffusivities up to 6 to 10 orders of magnitude faster between 700−300 °C. No matter how approximate, these estimates quantitatively constrain the range of ^{40}Ar transport rates in natural, undeformed, muscovite affected by coupled chemical-nanostructural transformations of the interlayer.

ACKNOWLEDGEMENTS

Work supported by LABEX grant VOLTAIRE (ANR-10-LABX-100-01), the Région Centre grant ARGON, and the EQUIPEX grant PLANEX (ANR-11-EQPX-0036). J. Nteme is supported by a post-doctoral grant from the project LABEX-VOLTAIRE. Kip Hodges (NG3L, ASU) and two anonymous reviewers provided perceptive and really motivating reviews that helped to improve the final version. Associate Editor C. Gautheron is thanked for efficient ms handling while on the move to Grenoble. The material and ideas developed in this paper form the basis of the project "DeconVar" discarded as "*unlikely to lead to a breakthrough and widespread application of the findings*" by the ANR screening committee CE49 "Planétologie, structure et histoire de la Terre" (2021 AAPG call; K. Kuiper, $^{40}Ar/^{39}Ar$ panel member).

REFERENCES

Ahn J. H., Peacor D. R. and Essene E. J. (1986) Cation-diffusion-induced characteristic beam damage in transmission electron microscope images of micas. *Ultramicroscopy* **19**, 375-381.

Ahn J. H. and Buseck P. R. (1998) Transmission electron microscopy of muscovite alteration of tourmaline. *Am. Mineral.* **83**, 535-541.

Amouric M. (1987) Growth and deformation defects in phyllosilicates as seen by HRTEM. *Acta Crystallo. Sec. B: Struct. Sci.* **43**, 57-63.

Aslin J., Mariani E., Dawson K. and Barsoum M. W. (2019) Ripplocations provide a new mechanism for the deformation of phyllosilicates in the lithosphere. *Nature com.* **10**, 1-9.

Beaudoin A., Scaillet S., Mora N., Jolivet L. and Augier R. (2020) In Situ and Step-Heating $^{40}Ar/^{39}Ar$ Dating of White Mica in Low-Temperature Shear Zones (Tenda Massif, Alpine Corsica, France). *Tectonics* **39**, e2020TC006246.

Berry J., Duke E. and Snee L. (1994) $^{40}Ar/^{39}Ar$ thermochronology of Precambrian metamorphic rocks of the Harney Peak granite, Black Hills, South Dakota. In *Geological Society of America Abstracts with Programs* Geological Society of America Abstracts with Programs. p. 4.

Boundy T. M., Hall C. M., Li G., Essene E. J. and Halliday A. (1997) Fine-scale isotopic heterogeneities and fluids in the deep crust: a $^{40}Ar/^{39}Ar$ laser ablation and TEM study of muscovite from a granulite-eclogite transition zone. *Earth Planet. Sci. Lett.* **148**, 223-242.

Camacho A., Lee J., Fitzgerald J., Zhao J., Abdu Y.A., Jenkins D.M., Hawthorne F.C., Kyser T.K., Creaser R.A., Armstrong R., Heaman L.W. (2012) Planar defects as Ar traps in trioctahedral micas: A mechanism for increased Ar retentivity in phlogopite. *Earth Planet. Sci. Lett.* **341**, 255-267.

Capitani G., Schingaro E., Lacalamita M., Mesto E. and Scordari F. (2016) Structural anomalies in tobelite-2M_2 explained by high resolution and analytical electron microscopy. *Mineral. Mag.* **80**, 143-156.

Chamberlain K.R., Frost C.D. and Frost B.R. (2003) Eartly Archean to Mesoproterozoic evolution of the Wyoming Province: Archean origins to modern lithospheric structure. *Canadian J. of Earth Sci* **40**, 1357-1374.

Dahl P. S. (1996) The crystal-chemical basis for Ar retention in micas: inferences from interlayer partitioning and implications for geochronology. *Contrib. Miner. Petrol.* **123(1)**, 22-39.

Dahl P. S., Holm D. K., Gardner E. T., Hubacher F. A. and Foland K. A. (1999) New constraints on the timing of Early Proterozoic tectonism in the Black Hills (South Dakota), with implications for docking of the Wyoming province with Laurentia. *Geol. Soc. Am. Bul.* **111**, 1335-1349.

Dahl P. S., Hamilton M. A., Jercinovic M. J., Terry M. P., Williams M. L. and Frei R. (2005) Comparative isotopic and chemical geochronometry of monazite, with implications for U-Th-Pb dating by electron microprobe: An example from metamorphic rocks of the eastern Wyoming Craton (USA). *Am. Mineral.* **90**, 619-638.

Dahl P. S. and Foland K. A. (2008) Concentric slow cooling of a low-P-high-T terrane: Evidence from 1600-1300 Ma mica dates in the 1780-1700 Ma Black Hills Orogen, South Dakota, USA. *Am. Mineral.* **93**, 1215-1229.

Deino A. and Potts R. (1992) Age-probability spectra for examination of single-crystal $^{40}Ar/^{39}Ar$ dating results: Examples from Olorgesailie, southern Kenya Rift. *Quater. Inter.* **13**, 47-53.

de Jong K., Wijbrans J. R. and Féraud G. (1992) Repeated thermal resetting of phengites in the Mulhacen Complex (Betic Zone, southeastern Spain) shown by $^{40}Ar/^{39}Ar$ step heating and single grain laser probe dating. *Earth Planet. Sci. Lett.* **110**, 173-191.

Di Vincenzo G., Ghiribelli B., Giorgetti G. and Palmeri R. (2001) Evidence of a close link between petrology and isotope records: constraints from SEM, EMP, TEM and in situ ^{40}Ar-^{39}Ar laser analyses on multiple generations of white micas (Lanterman Range, Antarctica). *Earth Planet. Sci. Lett.* **192**, 389-405.

Di Vincenzo G., Carosi R. and Palmeri R. (2004) The relationship between tectono-metamorphic evolution and argon isotope records in white mica: constraints from in situ ^{40}Ar-^{39}Ar laser

analysis of the Variscan basement of Sardinia. *J. Petrol.* **45**, 1013-1043.

Di Vincenzo G., Tonarini S., Lombardo B., Castelli D. and Ottolini L. (2006) Comparison of ^{40}Ar-^{39}Ar and Rb-Sr data on phengites from the UHP Brossasco-Isasca Unit (Dora Maira Massif, Italy): implications for dating white mica. *J. Petrol.* **47**, 1439-1465.

Duke E. F., Redden J. A. and Papike J. J. (1988) Calamity Peak layered granite-pegmatite complex, Black Hills, South Dakota: Part I. Structure and emplacement. *Geol. Soc. Am. Bul.* **100**, 825-840.

Fornash K. F., Cosca M. A. and Whitney D. L. (2016) Tracking the timing of subduction and exhumation using ^{40}Ar/^{39}Ar phengite ages in blueschist-and eclogite-facies rocks (Sivrihisar, Turkey). *Contrib. Miner. Petrol.* **171**, 1-37.

Forster M. A. and Lister G. S. (2014) ^{40}Ar/^{39}Ar geochronology and the diffusion of ^{39}Ar in phengite–muscovite intergrowths during step-heating experiments in vacuo. *Geol. Soc., Lond., Spec. Publ.* **378**, 117–135.

Gaber L. J., Foland K. A. and Corbato, C. E. (1988) On the significance of argon release from biotite and amphibole during ^{40}Ar/^{39}Ar vacuum heating. *Geochim. Cosmochim. Acta* **52**, 2457-2465.

Giletti B. J., Hofmann A., Yoder H. and Yund R. (1974) Studies in diffusion I: argon in phlogopite mica. *In Geochemical transport and kinetics Geochemical transport and kinetics.* Carnegie Institution of Washington Washington, DC. pp. 107-115.

Giorgetti G., Tropper P., Essene E. J. and Peacor D. R. (2000) Characterization of non-equilibrium and equilibrium occurrences of paragonite/muscovite intergrowths in an eclogite from the Sesia-Lanzo Zone (Western Alps, Italy). *Contrib. Miner. Petrol.* **138**, 326-336.

Goodwin L. B. and Wenk H.-R. (1990) Intracrystalline folding and cataclasis in biotite of the Santa Rosa mylonite zone: HVEM and TEM observations. *Tectonophysics* **172**, 201-214.

Grove M. and Harrison T. M. (1996) ^{40}Ar* diffusion in Fe-rich biotite. *Am. Min.* **81**, 940–951.

905 Guidotti C. V. (1984) Micas in metamorphic rocks. *Rev. mineral. geochem.* **13**, 357-467.

906 Hames W. and Hodges K. (1993) Laser $^{40}Ar/^{39}Ar$ evaluation of slow cooling and episodic loss of
907 ^{40}Ar from a sample of polymetamorphic muscovite. *Science* **261**, 1721-1723.

908 Hames W. and Bowring S. (1994) An empirical evaluation of the argon diffusion geometry in mus-
909 covite. *Earth Planet. Sci. Lett.* **124**, 161-169.

910 Hames W. E. and Cheney J. (1997) On the loss of ^{40}Ar from muscovite during polymetamorphism.
911 *Geochim. Cosmochim. Acta* **61**, 3863-3872.

912 Hames W. E., Cheney J. T. and Tracy R. J. (2008) Single-crystal $^{40}Ar/^{39}Ar$ age variation in
913 muscovite of the Gassetts Schist and associated gneiss, Vermont Appalachians. *Am. Mineral.*
914 **93**, 384-395.

915 Harrison T. M., Duncan I. and Mcdougall I. (1985) Diffusion of ^{40}Ar in biotite: temperature,
916 pressure and compositional effects. *Geochim. Cosmochim. Acta* **49**, 2461-2468.

917 Harrison T. M., Célérier J., Aikman A. B., Hermann J. and Heizler M. T. (2009) Diffusion of ^{40}Ar
918 in muscovite. *Geochim. Cosmochim. Acta* **73**, 1039-1051.

919 Hart E. W. (1957) On the role of dislocations in bulk diffusion. *Acta metal.* **5**, 597.

920 Hodges K. V., Harries W. E. and Bowring S. A. (1994) $^{40}Ar/^{39}Ar$ age gradients in micas from
921 a high-temperature-low-pressure metamorphic terrain: Evidence for very slow cooling and
922 implications for the interpretation of age spectra. *Geology* **22**, 55-58.

923 Hodges K. and Bowring S. (1995) $^{40}Ar/^{39}Ar$ thermochronology of isotopically zoned micas: Insights
924 from the southwestern USA proterozoic orogen. *Geochim. Cosmochim. Acta* **59**, 3205-3220.

925 Holm D. K., Dahl P. S. and Lux D. R. (1997) $^{40}Ar/^{39}Ar$ evidence for Middle Proterozoic (1300-1500
926 Ma) slow cooling of the southern Black Hills, South Dakota, midcontinent, North America:
927 Implications for Early Proterozoic P-T evolution and posttectonic magmatism. *Tectonics* **16**,
928 609-622.

929 Kellett D. A., Warren C., Larson K. P., Zwingmann H., van Staal C. R. and Rogers N. (2016)
930 Influence of deformation and fluids on Ar retention in white mica: Dating the Dover Fault,
931 Newfoundland Appalachians. *Lithos* **254**, 1-17.

932 Kelley S., Reddy S. and Maddock R. (1994) Laser-probe $^{40}Ar/^{39}Ar$ investigation of a pseudotachy-
933 lyte and its host rock from the Outer Isles thrust, Scotland. *Geology* **22**, 443-446.

934 Kelley S. and Wartho J. (2000) Rapid kimberlite ascent and the significance of Ar-Ar ages in xenolith
935 phlogopites. *Science* **289**, 609-611.

936 Kirschner D. L., Cosca M. A., Masson H. and Hunziker J. C. (1996) Staircase $^{40}Ar/^{39}Ar$ spectra
937 of fine-grained white mica: Timing and duration of deformation and empirical constraints on
938 argon diffusion. *Geology* **24**, 747-750.

939 Kramar N., Cosca M. A. and Hunziker J. C. (2001) Heterogeneous $^{40}Ar^{*}$ distributions in natu-
940 rally deformed muscovite: in situ UV-laser ablation evidence for microstructurally controlled
941 intragrain diffusion. *Earth Planet. Sci. Lett.* **192**, 377-388.

942 Kramar N. (2002) Microstructural controls on intragranular argon diffusion in naturally deformed
943 muscovite. Doctoral dissertation, University of Lausanne.

944 Kramar N., Cosca M. A., Buffat P.-A. and Baumgartner L. P. (2003) Stacking fault-enhanced argon
945 diffusion in naturally deformed muscovite. *Geol. Soc., Lond., Spec. Publ.* **220**, 249-260.

946 Krogstad E. J. and Walker R. J. (1994) High closure temperatures of the U-Pb system in large
947 apatites from the Tin Mountain pegmatite, Black Hills, South Dakota, USA. *Geochim. Cos-*
948 *mochim. Acta* **58**, 3845-3853.

949 Laurent V., Scaillet S., Jolivet L., Augier R. and Roche V. (2021) ^{40}Ar behaviour and exhuma-
950 tion dynamics in a subduction channel from multi-scale $^{40}Ar/^{39}Ar$ systematics in phengite.
951 *Geochim. Cosmochim. Acta* **311**, 141-173.

952 Lee J. K. (1993) The argon release mechanisms of hornblende in vacuo. *Chem. Geol.* **106**, 133–170.

953 Lee J. K. (1995) Multipath diffusion in geochronology. *Contrib. Miner. Petrol.* **120**, 60-82.

954 Lisenbee A. L. (1978) South Dakota-Wyoming-Montana. Laramide folding associated with base-
955 ment block faulting in the western United States. *Geol. Soc. Am. Mem.* **151**, 165-169.

956 Livi K. J., Christidis G. E., Árkai P. and Veblen D. R. (2008) White mica domain formation: A
957 model for paragonite, margarite, and muscovite formation during prograde metamorphism.
958 *Am. Mineral.* **93**, 520-527.

959 Lovera O. M., Richter F. M. and Harrison T. M. (1989) The $^{40}Ar/^{39}Ar$ thermochronometry for
960 slowly cooled samples having a distribution of diffusion domain sizes. *J. Geophys. Res. Solid*
961 *Earth* **94**, 17917-17935.

962 Mehrer H. (2007) *Diffusion in solids: fundamentals, methods, materials, diffusion-controlled pro-*
963 *cesses.*, Springer Science & Business Media.

964 Merriman R., Roberts B. and Peacor D. (1990) A transmission electron microscope study of white
965 mica crystallite size distribution in a mudstone to slate transitional sequence, North Wales,
966 UK. *Contrib. Miner. Petrol.* **106**, 27-40.

967 Mulch A., Cosca M. and Handy M. (2002) In-situ UV-laser $^{40}Ar/^{39}Ar$ geochronology of a micaceous
968 mylonite: an example of defect-enhanced argon loss. *Contrib. Miner. Petrol.* **142**, 738-752.

969 Mulch A. and Cosca M. A. (2004) Recrystallization or cooling ages: in situ UV-laser $^{40}Ar/^{39}Ar$
970 geochronology of muscovite in mylonitic rocks. *J. Geol. Soc.* **161**, 573-582.

971 Mulch A., Cosca M., Andresen A. and Fiebig J. (2005) Time scales of deformation and exhumation
972 in extensional detachment systems determined by high-spatial resolution in situ UV-laser
973 $^{40}Ar/^{39}Ar$ dating. *Earth Planet. Sci. Lett.* **233**, 375-390.

974 Mulch A., Teyssier C., Cosca M. and Vennemann T. (2006) Thermomechanical analysis of strain
975 localization in a ductile detachment zone. *J. Geophys. Res. Solid Earth* **111**.

976 Nabelek P. I., Russ-Nabelek C. and Denison J. (1992a) The generation and crystallization conditions
977 of the Proterozoic Harney Peak leucogranite, Black Hills, South Dakota, USA: petrologic and
978 geochemical constraints. *Contrib. Miner. Petrol.* **110**, 173–191.

Nabelek P. I., Russ-Nabelek C. and Haeussler G. (1992b) Stable isotope evidence for the petrogenesis and fluid evolution in the Proterozoic Harney Peak leucogranite, Black Hills, South Dakota. *Geochim. Cosmochim. Acta* **56**, 403-417.

Nabelek P. I. and Ternes K. (1997) Fluid inclusions in the Harney Peak Granite, Black Hills, South Dakota, USA: Implications for solubility and evolution of magmatic volatiles and crystallization of leucogranite magmas. *Geochim. Cosmochim. Acta* **61**, 1447-1465.

Nabelek P. I., Sirbescu M. and Liu M. (1999) Petrogenesis and tectonic context of the Harney Peak Granite, Black Hills, South Dakota. *Rocky Mount. Geol.* **34**, 165-181.

Nabelek P. I., Labotka T. C., Helms T. and Wilke M. (2006) Fluid-mediated polymetamorphism related to Proterozoic collision of Archean Wyoming and Superior provinces in the Black Hills, South Dakota. *Am. Miner.* **91**, 1473–1487.

Nabelek P. I., Whittington A. G. and Sirbescu M.-L. C. (2010) The role of H_2O in rapid emplacement and crystallization of granite pegmatites: resolving the paradox of large crystals in highly undercooled melts. *Contrib. Miner. Petrol.* **160**, 313–325.

Nabelek P. and Chen Y. (2014) The initial garnet-in reaction involving siderite–rhodochrosite, garnet re-equilibration and P–T–t paths of graphitic schists in the Black Hills orogen, South Dakota, USA. *J. metam. Geol.* **32**, 133–150.

Neusser G., Abart R., Fischer F. D., Harlov D. and Norberg N. (2012) Experimental Na/K exchange between alkali feldspar and an NaCl-KCl salt melt: chemically induced fracturing and element partitioning. *Contrib. Miner. Petrol.* **164**, 341-358.

Norwood C. B. (1974) Radiogenic argon diffusion in the biotite micas. Brown University.

Nteme J. (2021) Diffusion de l'argon dans les micas : calibration empirique et simulations atomistiques. Doctoral dissertation, University of Orleans.

Nteme J., Scaillet S., Brault P., Tassan-Got L. (2022) Atomistic Simulations of ^{40}Ar Diffusion in Muscovite. *Geochim. Cosmochim. Acta* **331**, 123-142.

1004 Onstott T. C., Phillips D. and Pringle-Goodell L. (1991) Laser microprobe measurement of chlorine
1005 and argon zonation in biotite. *Chem. Geol.* **90**, 145-168.

1006 Petrishcheva E., Rieder M., Predan J., Fischer F. D., Giester G. and Abart R. (2019) Diffusion-
1007 controlled crack propagation in alkali feldspar. *Phys. chem. miner.* **46**, 15-26.

1008 Phillips D. and Onstott T. C. (1988) Argon isotopic zoning in mantle phlogopite. *Geology* **16**,
1009 542-546.

1010 Phillips D. (1991) Argon isotope and halogen chemistry of phlogopite from South African kim-
1011 berlites: a combined step-heating, laser probe, electron microprobe and TEM study. *Chem.*
1012 *Geol.: Isotope Geosc. Sec.* **87**, 71-98.

1013 Pickles C., Kelley S., Reddy S. and Wheeler J. (1997) Determination of high spatial resolution argon
1014 isotope variations in metamorphic biotites. *Geochim. Cosmochim. Acta* **61**, 3809-3833.

1015 Putlitz B., Cosca M. and Schumacher J. (2005) Prograde mica $^{40}Ar/^{39}Ar$ growth ages recorded in
1016 high pressure rocks (Syros, Cyclades, Greece). *Chem. Geol.* **214**, 79-98.

1017 Radoslovich E. (1960) The structure of muscovite, KAl_2 $(Si_3Al)O_{10}(OH)_2$. *Acta Crystallo.* **13**,
1018 919-932.

1019 Ratté, J.C. (1986) Geologic map of the Medicine Mountain Quadrangle, Pennington County, South
1020 Dakota. United States Geological Survey Miscellaneous Investigation Series Map I-1654, scale
1021 1:24,000.

1022 Redden J. A., Peterman Z., Zartman R., DeWitt E., Lewry J. and Stauffer M. (1990) U-Th-Pb
1023 geochronology and preliminary interpretation of Precambrian tectonic events in the Black
1024 Hills, South Dakota. In *The Early Proterozoic Trans-Hudson Orogen of North America (ed.*
1025 *J. F. Lewry and M. R. Stauffer); Geol. Assoc. Canada Spec. Paper* **37**, 229-51.

1026 Renne P. R., Swisher C. C., Deino A. L., Karner D. B., Owens T. L. and DePaolo D. J. (1998)
1027 Intercalibration of standards, absolute ages and uncertainties in $^{40}Ar/^{39}Ar$ dating. *Chem.*
1028 *Geol.* **145**, 117-152.

1029 Riley G. (1970) Isotopic discrepancies in zoned pegmatites, Black Hills, South Dakota. *Geochim.*
1030 *Cosmochim. Acta* **34**, 713-725.

1031 Robbins C. (1972) Radiogenic argon diffusion in muscovite under hydrothermal conditions. M. Sc.
1032 Thesis, Brown Univ., Providence, RI.

1033 Rosenbaum G., Menegon L., Glodny J., Vasconcelos P., Ring U., Massironi M., Thiede D. and
1034 Nasipuri P. (2012) Dating deformation in the Gran Paradiso Massif (NW Italian Alps): Im-
1035 plications for the exhumation of high-pressure rocks in a collisional belt. *Lithos* **144**, 130-144.

1036 Scaillet S., Féraud G., Lagabrielle Y., Ballèvre M. and Ruffet G. (1990) $^{40}Ar/^{39}Ar$ laser-probe dating
1037 by step heating and spot fusion of phengites from the Dora Maira nappe of the western Alps,
1038 Italy. *Geology* **18**, 741-744.

1039 Scaillet S., Féraud G., Ballèvre M. and Amouric M. (1992) MgFe and [(Mg,Fe)Si-Al_2] compositional
1040 control on argon behaviour in high-pressure white micas: A $^{40}Ar/^{39}Ar$ continuous laser-probe
1041 study from the Dora-Maira nappe of the internal western Alps, Italy. *Geochim. Cosmochim.*
1042 *Acta* **56**, 2851-2872.

1043 Scaillet S., Cheilletz A., Cuney M., Farrar E. and Archibald D. (1996) Cooling pattern and mineral-
1044 ization history of the Saint Sylvestre and western Marche leucogranite pluton, French Massif
1045 Central: I. $^{40}Ar/^{39}Ar$ isotopic constraints. *Geochim. Cosmochim. Acta* **60**, 4653-4671.

1046 Scaillet S. (1998) K-Ar ($^{40}Ar/^{39}Ar$) geochronology of ultrahigh pressure rocks. In *When continents*
1047 *collide: Geodynamics and geochemistry of ultrahigh-pressure rocks.* Springer. pp. 161-201.

1048 Scaillet S. (2000) Numerical error analysis in $^{40}Ar/^{39}Ar$ dating. *Chem. Geol.* **162**, 269-298.

1049 Scharf A., Handy M. R., Schmid S. M., Favaro S., Sudo M., Schuster R. and Hammerschmidt K.
1050 (2016) Grain-size effects on the closure temperature of white mica in a crustal-scale extensional
1051 shear zone-Implications of in-situ $^{40}Ar/^{39}Ar$ laser-ablation of white mica for dating shearing
1052 and cooling (Tauern Window, Eastern Alps). *Tectonophysics* **674**, 210-226.

1053 Scheidl K., Schaeffer A. K., Petrishcheva E., Habler G., Fischer F. D., Schreuer J. and Abart R.
1054 (2014) Chemically induced fracturing in alkali feldspar. *Phys. chem. miner.* **41**, 1-16.

1055 Schneider S., Hammerschmidt K. and Rosenberg C. L. (2013) Dating the longevity of ductile shear
1056 zones: Insight from $^{40}Ar/^{39}Ar$ in situ analyses. *Earth Planet. Sci. Lett.* **369**, 43-58.

1057 Shau Y.-H., Feather M. E., Essene E. J. and Peacor D. R. (1991) Genesis and solvus relations of sub-
1058 microscopically intergrown paragonite and phengite in a blueschist from northern California.
1059 *Contrib. Miner. Petrol.* **106**, 367-378.

1060 Sio C. K. I., Dauphas N., Teng F. Z., Chaussidon M., Helz R. T. and Roskosz M. (2013) Discerning
1061 crystal growth from diffusion profiles in zoned olivine by in situ Mg-Fe isotopic analyses.
1062 *Geochim. Cosmochim. Acta* **123**, 302-321.

1063 Sirbescu M.-L. C. and Nabelek P. I. (2003) Crystallization conditions and evolution of magmatic
1064 fluids in the Harney Peak Granite and associated pegmatites, Black Hills, South Dakota-
1065 Evidence from fluid inclusions. *Geochim. Cosmochim. Acta* **67**, 2443-2465.

1066 Skipton D., Schneider D., Kellett D. and Joyce N. (2017) Deciphering the Paleoproterozoic cooling
1067 history of the northeastern Trans-Hudson Orogen, Baffin Island (Canada), using $^{40}Ar/^{39}Ar$
1068 step-heating and UV laser thermochronology. *Lithos* **284**, 69-90.

1069 Sletten V. W. and Onstott A. T. (1998) The effect of the instability of muscovite during in vacuo
1070 heating on $^{40}Ar/^{39}Ar$ step-heating spectra. *Geochim. Cosmochim. Acta* **62**, 123-141.

1071 Smith S., Kelley S., Tindle A. and Breaks F. (2005) Compositional controls on $^{40}Ar/^{39}Ar$ ages of
1072 zoned mica from a rare-element pegmatite. *Contrib. Miner. Petrol.* **149**, 613-626.

1073 Steiger R. H. and Jæger E. (1977) Subcommission on geochronology: convention on the use of decay
1074 constants in geo-and cosmochronology. *Earth Planet. Sci. Lett.* **36**, 359-362.

1075 Veblen D. R. (1983) Microstructures and mixed layering in intergrown wonesite, chlorite, talc,
1076 biotite, and kaolinite. *Am. Mineral.* **68**, 566-580.

1077 Volfinger M. (1976) Effet de la température sur les distributions de Na, Rb et Cs entre la sanidine, la
1078 muscovite, la phlogopite et une solution hydrothermale sous une pression de 1 kbar. *Geochim.*
1079 *Cosmochim. Acta* **40**, 267–282.

1080 Webster J., Holloway J. and Hervig R. (1989) Partitioning of lithophile trace elements between H_2O
1081 and H_2O+ CO_2 fluids and topaz rhyolite melt. *Economic Geology* **84**, 116-134.

1082 Wells M. L., Spell T. L., Hoisch T. D., Arriola T. and Zanetti K. A. (2008) Laser-probe $^{40}Ar/^{39}Ar$
1083 dating of strain fringes: Mid-Cretaceous synconvergent orogen-parallel extension in the inte-
1084 rior of the Sevier orogen. *Tectonics* **27**.

1085 Whitney D. L. and Evans B. W. (2010) Abbreviations for names of rock-forming minerals. *Am.*
1086 *Mineral.* **95**, 185-187.

1087 Wiederkehr M., Sudo M., Bousquet R., Berger A. and Schmid S. M. (2009) Alpine orogenic evolution
1088 from subduction to collisional thermal overprint: The $^{40}Ar/^{39}Ar$ age constraints from the
1089 Valaisan Ocean, central Alps. *Tectonics* **28**.

1090 **TABLES**

Table 1: Location and mineralogy of dated samples. Mineral abbreviations after Whitney and Evans (2010).

Samples	Location	Mineralogy							GPS coordinate (WGS 84)	
		Qz	Ab	Mc	Ms	Bt	Tur	Grt	Latitude	Longitude
HP-10D	Central pluton	x	x	x	x		x		44.100000	-103.7555556
HP-13A	Central pluton	x	x	x	x		x		43.988889	-103.5888889
HP-45B	E. Sat. pluton	x	x	x	x		x	x	43.897500	-103.6102778
HP-2A	N. Sat. pluton	x	x	x	x		x	x	43.994444	-103.7388889
HP-34C	W. Sat. pluton	x	x	x	x		x		44.022778	-103.8044444

Table 2: HPG muscovite composition

Sample	HP-10D	HP-13A	HP-34C
SiO_2	46.17	46.54	48.19
TiO_2	0.19	0.11	0.18
Al_2O_3	34.23	34.61	34.78
FeO	1.7	1.67	1.42
MnO	0.04	0.02	0.03
MgO	0.63	0.54	0.65
Na_20	0.43	0.56	0.53
K_2O	10.71	10.47	10.52
F	0.05	0.07	0.00
Total	94.15	94.59	96.29
	Formula Basis 11 oxygens		
Si	3.12	3.13	3.17
AI(IV)	0.88	0.87	0.83
AI(Vl)	1.85	1.86	1.85
Ti	0.01	0.01	0.01
Fe	0.10	0.09	0.08
Mg	0.06	0.05	0.06
Mn	0.00	0.00	0.00
K	0.92	0.90	0.88
Na	0.06	0.07	0.07

Table 3: Cross-over ($1000/T_{xo}$; $\log D_{xo}$) point in Arrhenian space of best-fitting $E_v - D_0^v$ solution pairs matching the core age in muscovite *M11* of HP-10D (Fig. 16b) for the three thermal models considered in Fig. 15 assuming a range of activation energies between $E_v = 40-70$ kcal.mol^{-1}. Last columns block: examples of characteristic $E_v - D_0^v$ couples for the three cross-over families.

	$1000/T_{xo}$	$\log D_{xo}$	D_0^v (cm^2.s^{-1})			
Thermal model	(K^{-1})	(cm^2.s^{-1})	40*	50*	60*	70*
T_{min}	1.261	−18.70	2×10^{-8}	1×10^{-5}	7×10^{-3}	3
T_{mid}	1.147	−18.14	8×10^{-9}	3×10^{-6}	6×10^{-4}	3×10^{-1}
T_{max}	1.097	−18.30	2×10^{-9}	6×10^{-7}	1×10^{-4}	3×10^{-2}

* Activation energies (in kcal.mol^{-1})

Table 4: Empirical diffusion-domainal structure and diffusivities used in 2D modeling of defect-enhanced ^{40}Ar diffusion gradients (Fig. 17).

Grain	Domain	$\psi_d = f_{\mathrm{d}} D_0^{\mathrm{d}}$ ($\mathrm{cm}^2.\mathrm{s}^{-1}$)
HP-10D (*M11*)	1	3×10^{-5}
	2	1×10^{-6}
	3	2×10^{-4}
	4	6×10^{-5}
	5	2×10^{-5}
HP-13A (*M19*, split #1)	1	6×10^{-4}
	2	6×10^{-6}
	3	1×10^{-3}
	4	3×10^{-3}
	5	2×10^{-3}
HP-13A (*M19*, split #2)	1	3×10^{-4}
	2	6×10^{-6}
	3	5×10^{-4}
	4	5×10^{-4}
HP-13A (*M21*, split #2)	1	3×10^{-4}
	2	2×10^{-6}
	3	2×10^{-2}
	4	6×10^{-6}
	5	2×10^{-4}
	6	6×10^{-6}

FIGURES CAPTIONS

Fig. 1. Geological map of the southern part of the Black Hills (South Dakota, USA). Inset shows location of the mostly Proterozoic core of the Black Hills relative to regional lithotectonic domains. Abbreviations: WC and SC = Wyoming and Superior cratons; CPO/YAV = Central Plains (Yavapai) orogen; THO and BHO = Trans-Hudson and Black Hills orogens; BMD and HPD = Bear Mountain and Harney Peak domes; MT, WY, NE, ND, and SD = Montana, Wyoming, Nebraska, North and South Dakota, respectively. Modified from Dahl and Foland (2008).

Fig. 2. Thin section photomicrographs of selected samples. Automorphic muscovite crystals in samples HP-10D (a) and HP-13A (b). Muscovite aggregates in the sample HP-2A (c). Resorbed muscovite rims in samples HP-13A (d), HP-34C (e) and HP-2A (f). (g) Feldspars crystals devoid of inclusions (HP-13A). (h) Feldspars rich in inclusions (HP-34C).

Fig. 3. Optical microphotographs under crossed polars of muscovite grains selected for this study. Scale bar is 1 mm.

Fig. 4. SEM photograph of typical cone-shaped morphology and distribution of 35 μm wide 213-UV ablation pit along (001) in muscovite (sample HP-13A (*M19*) - #2).

Fig. 5. In situ $^{40}Ar/^{39}Ar$ mapping data in muscovite grains from HP-10D. Age contour maps reveal a conspicuous but irregular internal zoning, characterized by a consistent core-to-rim rejuvenation and the presence of a few isolated sub-cores retaining ages > 1.60 Ga. The dashed red line delimits peripherical delaminations. PDD curves plotted along with the IAF curves (see text for definitions). Both show consistent distributions. Scale bar is 1 mm. Age scale (color bar) with HPG intrusion age indicated.

Fig. 6. In situ $^{40}Ar/^{39}Ar$ mapping data in muscovite from HP-13A. All grains show a consistent age decrease towards the rims and the presence of a few sub-domains retaining

ages > 1.60 Ga. The dashed red line delimits peripherical delaminations. PDD and IAF curves show consistent distributions. Scale bar is 1 mm. Age scale (color bar) with HPG intrusion age indicated.

Fig. 7. In situ $^{40}Ar/^{39}Ar$ mapping data in muscovite from HP-45B (a) and HP-2A (b). Both grains show a rejuvenation towards the rims. The dashed red line delimits peripherical delaminations. PDD and IAF curves show consistent distributions. Scale bar is 1 mm. Age scale (color bar) with HPG intrusion age indicated.

Fig. 8. In situ $^{40}Ar/^{39}Ar$ mapping data in muscovite from HP-34C. All grains preserve ages older than the HPG crystallization age and show complex zoning patterns with younger zones all located on the rims. The dashed red line delimits peripherical delaminations. PDD and IAF curves show consistent distributions, except for grain *M4*. Scale bar is 1 mm. Age scale (color bar) with HPG intrusion age indicated.

Fig. 9. Compositional diagrams for three representative samples (HP-10D, HP-13A, HP-34C). Data from EMP analyses on thin sections. Notice marked Na_2O *vs.* K_2O anti-correlation for all three samples.

Fig. 10. EMP chemical profiles along (001) plane showing characteristic spatial compositional variations in representative samples (HP-13A and HP-34C). Observe anti-correlative variations of Na and K towards the rims.

Fig. 11. EDS chemical maps showing the spatial distribution of Na in HP-13A muscovite grains. Profiles A−B show a systematic core-to-rim decrease in Na content and an anti-correlative trend in K. Na profiles coincide in shape and first-order features with grain-scale $^{40}Ar/^{39}Ar$ variations extracted from *in situ* mapping (see age maps in Fig. 6).

Fig. 12. Microstructural TEM imaging of crystal zones selected based on $^{40}Ar/^{39}Ar$ distribution patterns. (a-c) STEM of FIB foils extracted perpendicular to (001) at locations

shown (stars) on the age contour and Na compositional maps. Notice the greater abundance of microstructural defects in Na-poor areas corresponding to younger $^{40}Ar/^{39}Ar$ ages. (d) Close-up TEM image (HP-10D, *M11*) revealing the defects as localized basal parting and delaminations (lenticular voids) up to 100−nm long parallel to (001); packets of layers sandwiched between planar defects display a characteristic mottled contrast.

Fig. 13. Substitutional relationship between Na and K in HPG muscovite. Red line: one-to-one (stoichiometric) exchange vector. ΔK and ΔNa calculated from data in profiles A−B shown in Fig. 10.

Fig. 14. Plot showing $^{40}Ar/^{39}Ar$ internal relationships in terms of age range and grain size. (a) Maximum recorded age versus percentage of defective zones (arbitrarily equated to age-map areas featuring ages younger than 1.5 Ga). Negative correlation suggests a continuum-diffusive scalar field interconnecting the cores with the edges. (b) Grain radius versus mean ages showing no correlation. (c) Maximum recorded ages versus shortest distance to rim showing lack of apparent correlation and suggesting ^{40}Ar transport through a non-uniform diffusive field.

Fig. 15. Model cooling curves used in numerical simulations. Data from Dahl and Foland (2008).

Fig. 16. Diffusion modeling results. (a) Arrhenian display of ^{40}Ar diffusion parameters allowing preservation of the intrusion age in the core of muscovite *M11* of HP-10D. Orange field contains all $E-D_0$ possible pairs, setting an upper bound to permissible ^{40}Ar diffusion rates in the absence of microstructural defects. Solid circles indicate cross-over points for the three thermal models T_{min} (blue), T_{mid} (red) and T_{max} (green). Line labeled "4": Arrhenian relationship derived from atomistic simulations for ideal muscovite (Nteme et al., 2022). Empirical and experimental estimates of Hames and Bowring (1994), Kirschner et al. (1996) and Harrison et al. (2009) as indicated. (b)

Core-to-rim profile (orange line) predicted from spatially-uniform 2D−diffusive modeling under the cooling displayed in Fig. 15 using the best-fitting $E-D_0$ pair in (a); note strong disparity with actual profile (purple line) measured across the grain (upper age map panel).

Fig. 17. Multi-path diffusion modeling results. Displayed for each grain are: i) the interpolated age map, ii) the diffusion-domain structure featuring the outline and number label referring to the domains reported in Table 4, iii) the synthetic age map, iv) a selected profile across (001) comparing theoretical 2D predictions with observed variations across (001).

Fig. 18. Arrhenius space of effective ^{40}Ar diffusion coefficient in HPG muscovite grains. The field in blue delimits ^{40}Ar diffusivity in the presence of microstructural defects. Published empirical and experimental diffusion estimates plot within this field, suggesting the presence of microstructural defects in the studied material. Stippled field: likely $D-T$ space spanned by ^{40}Ar kinetics in natural muscovite.

1197 **FIGURES**

Fig. 1

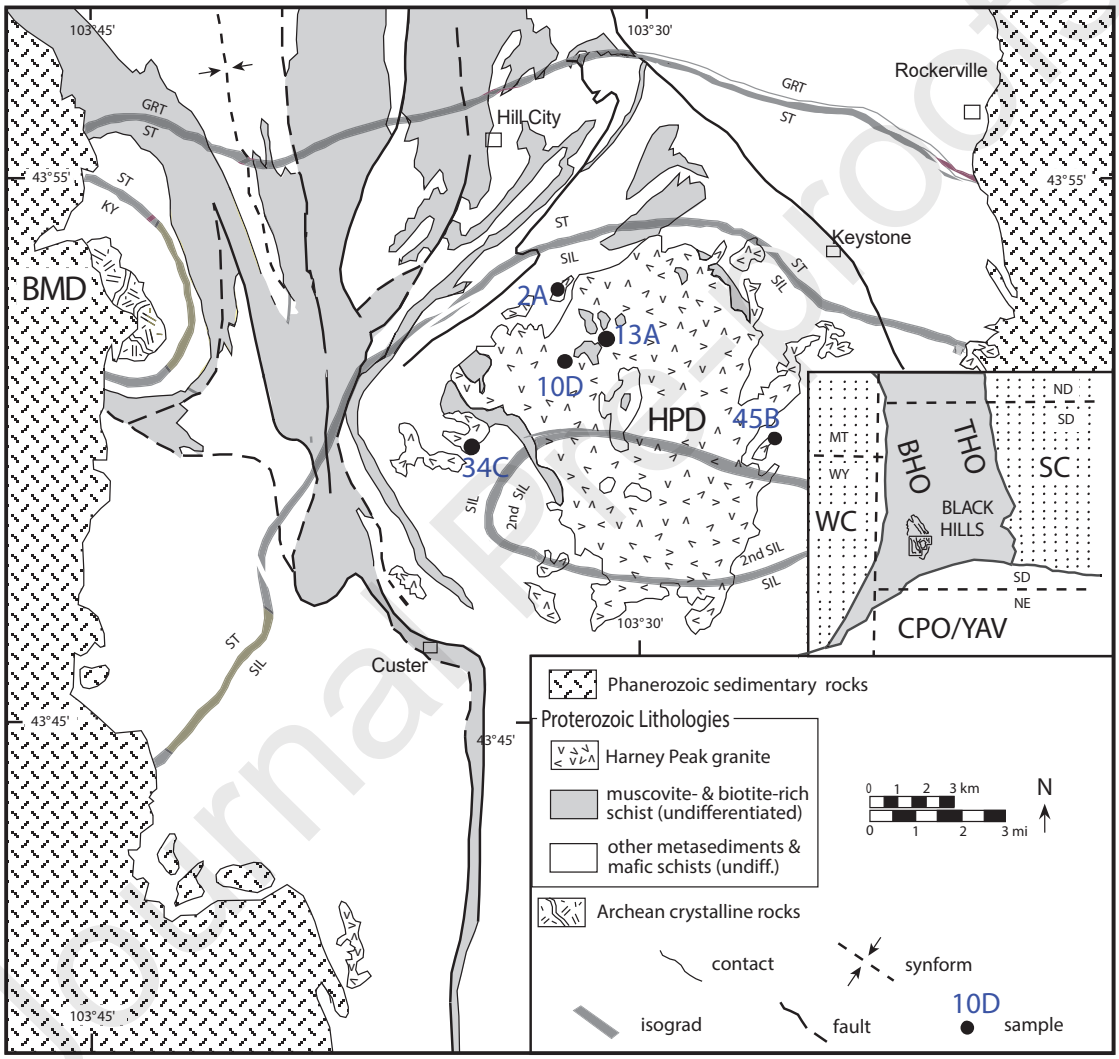

Fig. 2

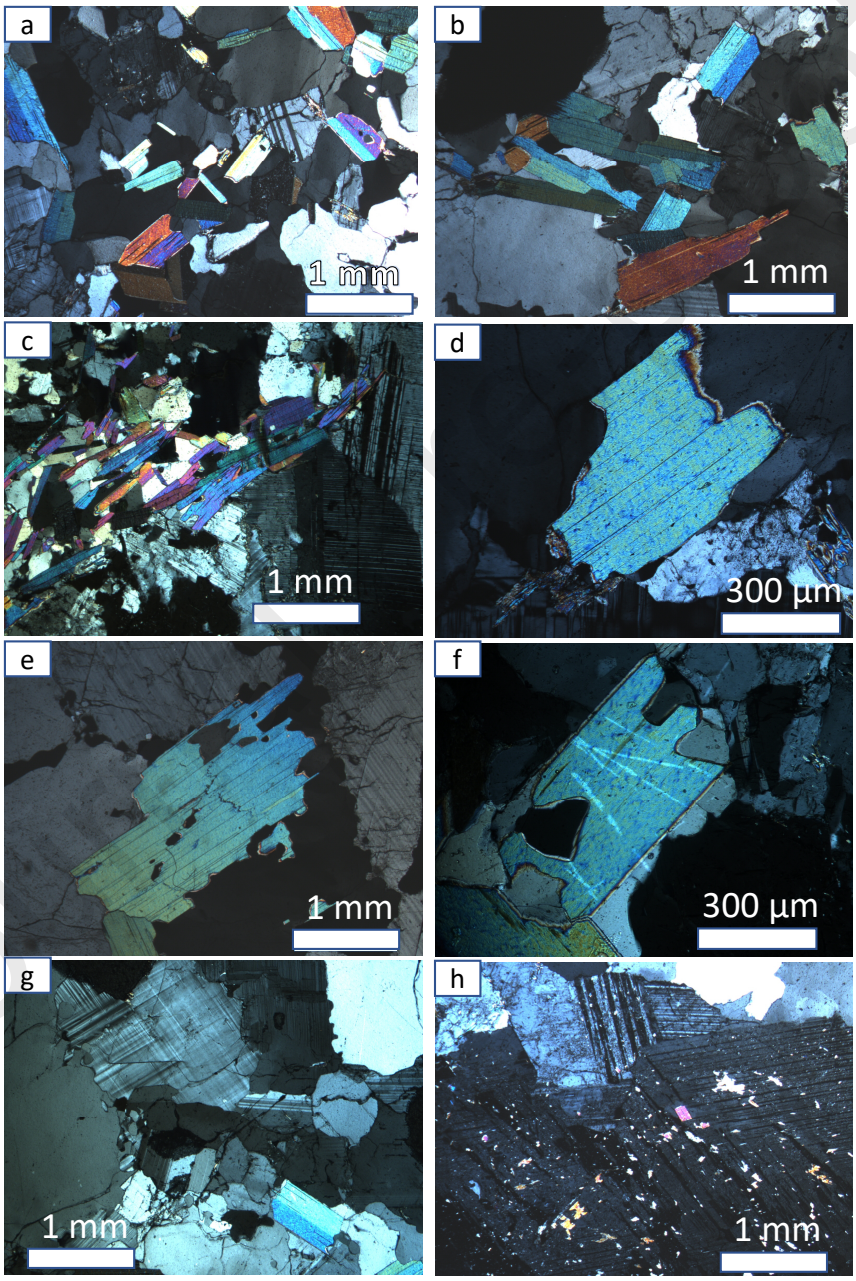

Fig. 3

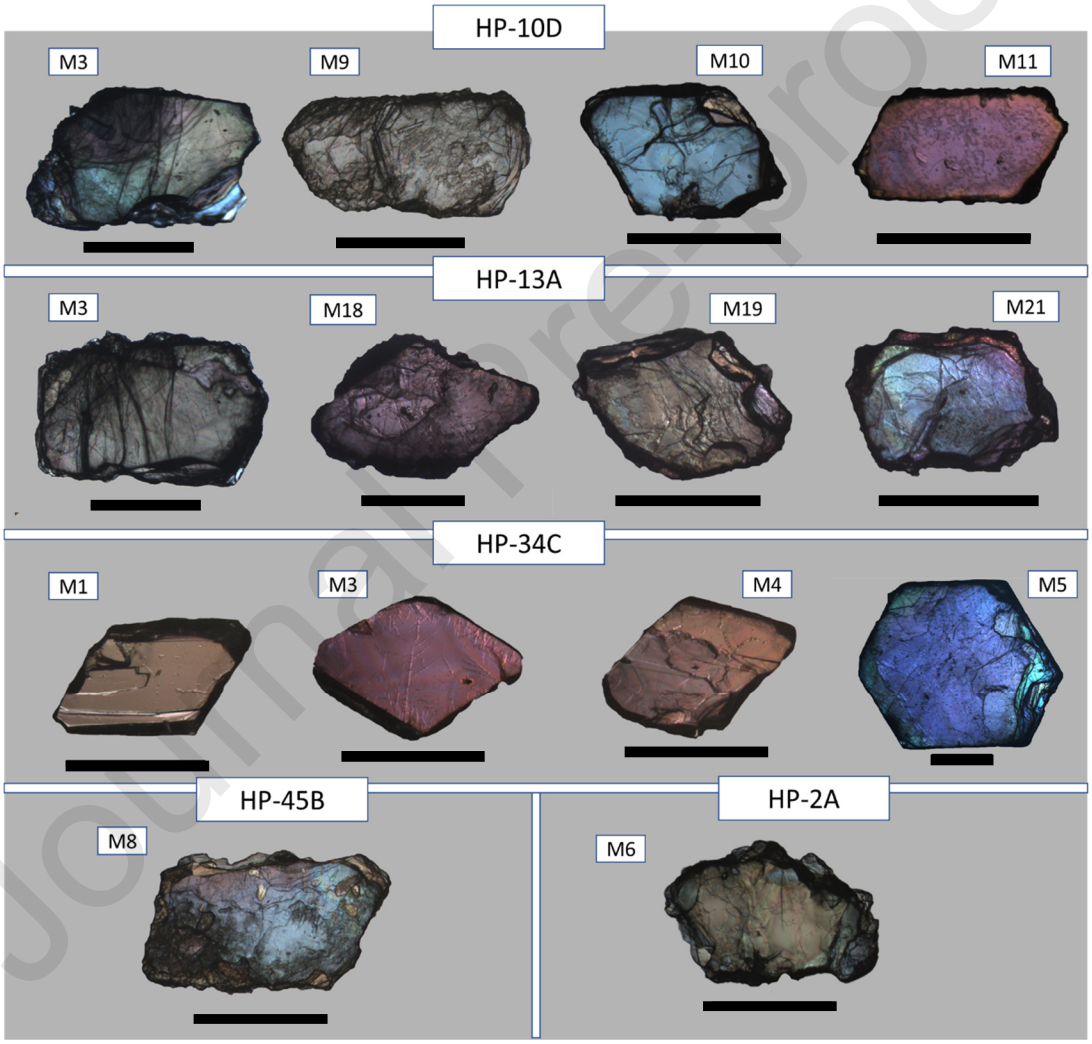

Fig. 4

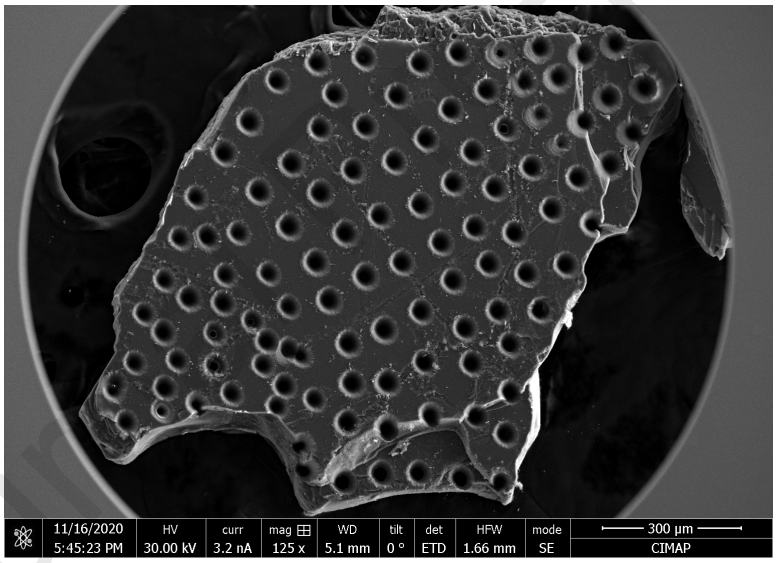

Fig. 5

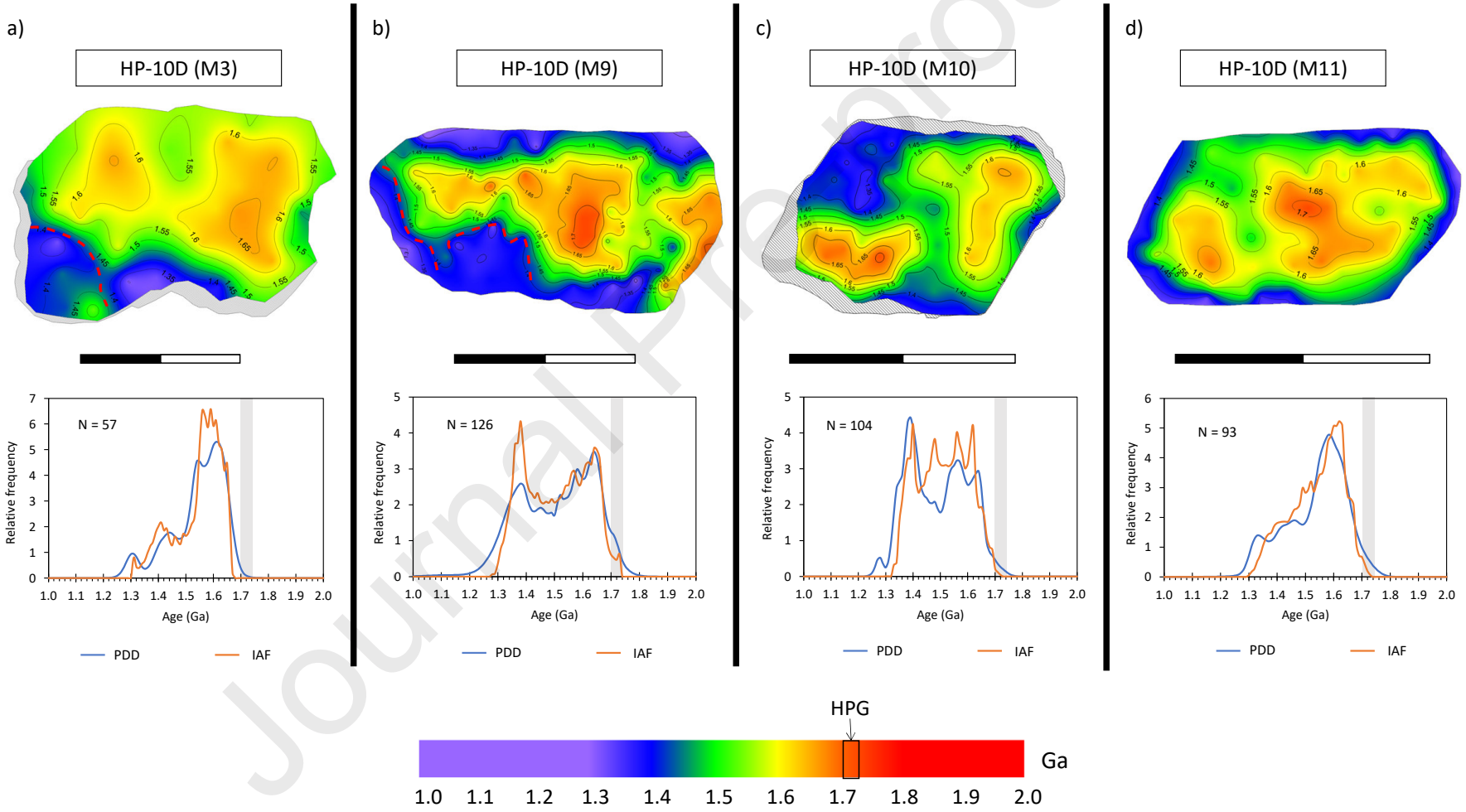

Fig. 6

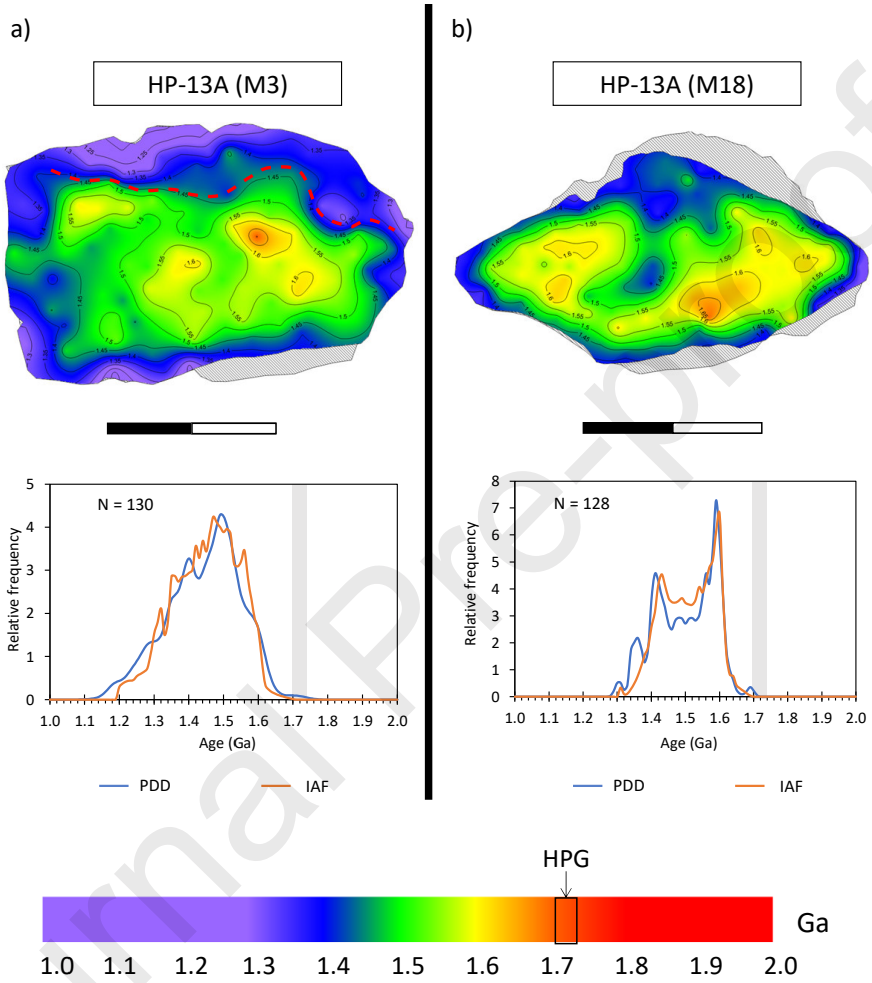

Fig. 6: (continued)

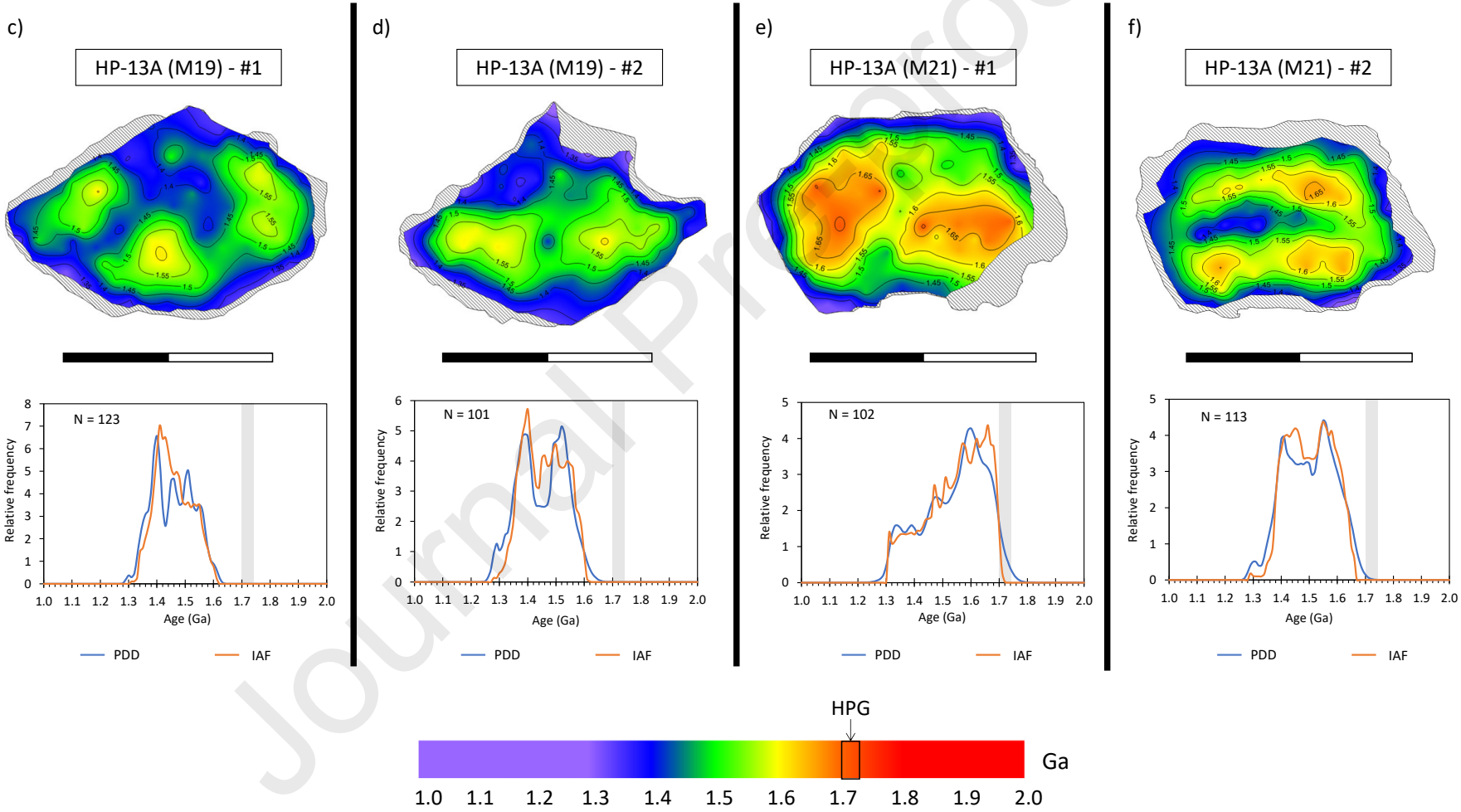

Fig. 7

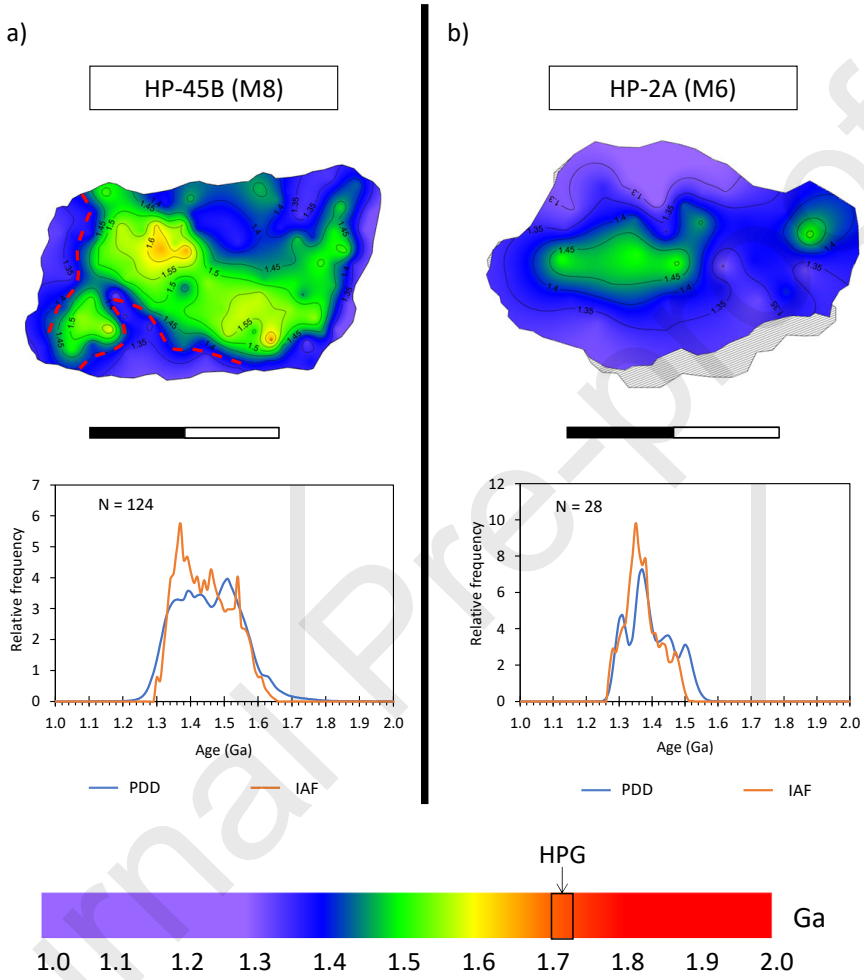

Fig. 8

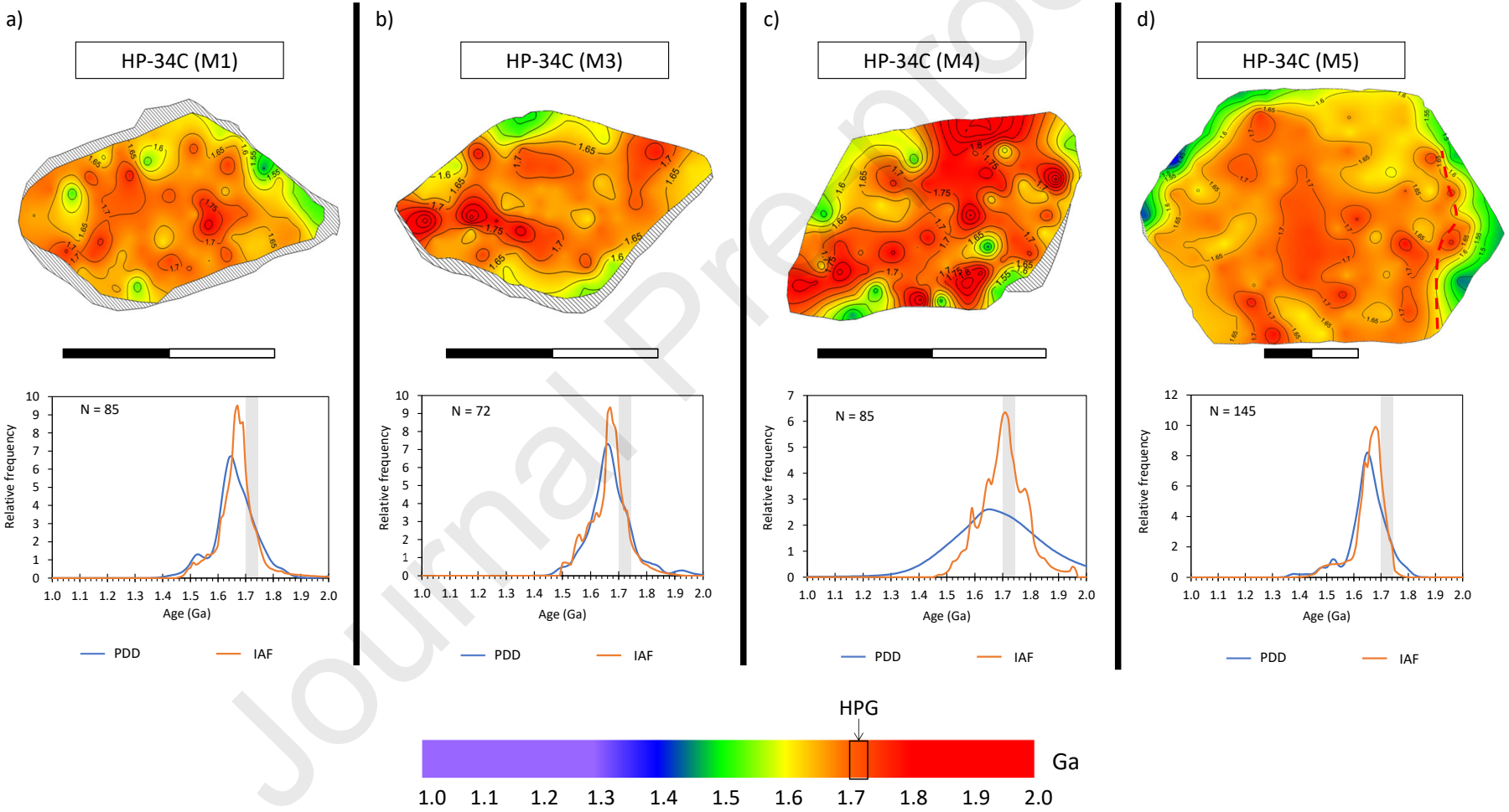

Fig. 9

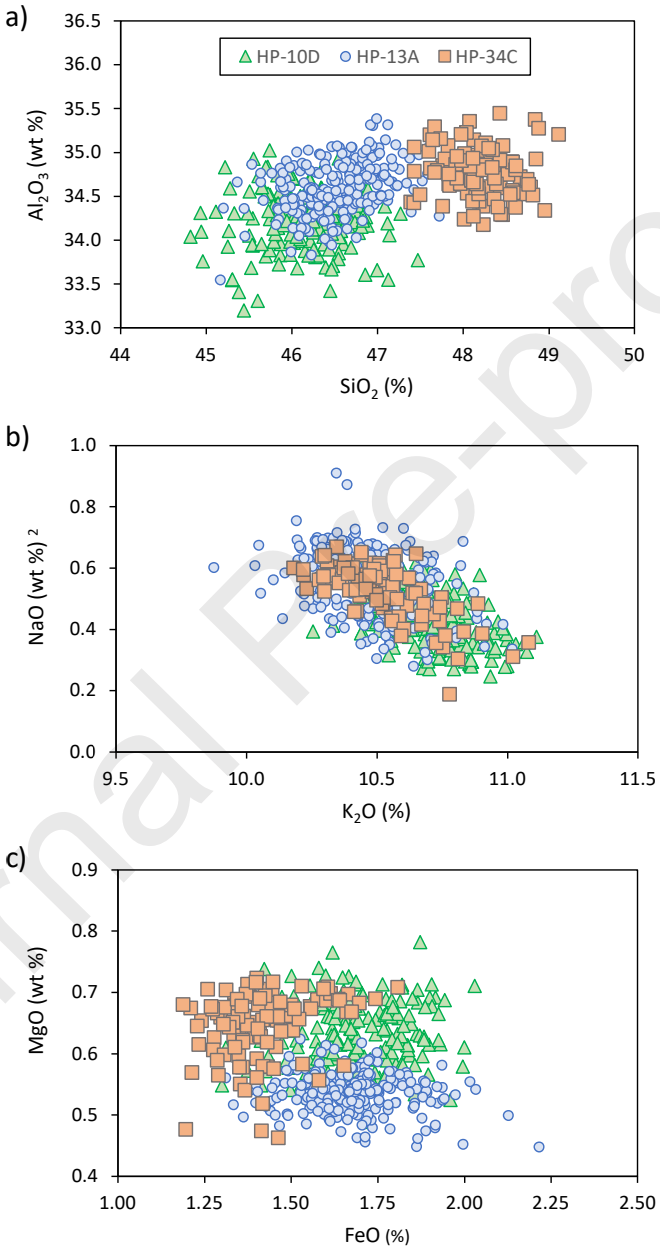

Fig. 10

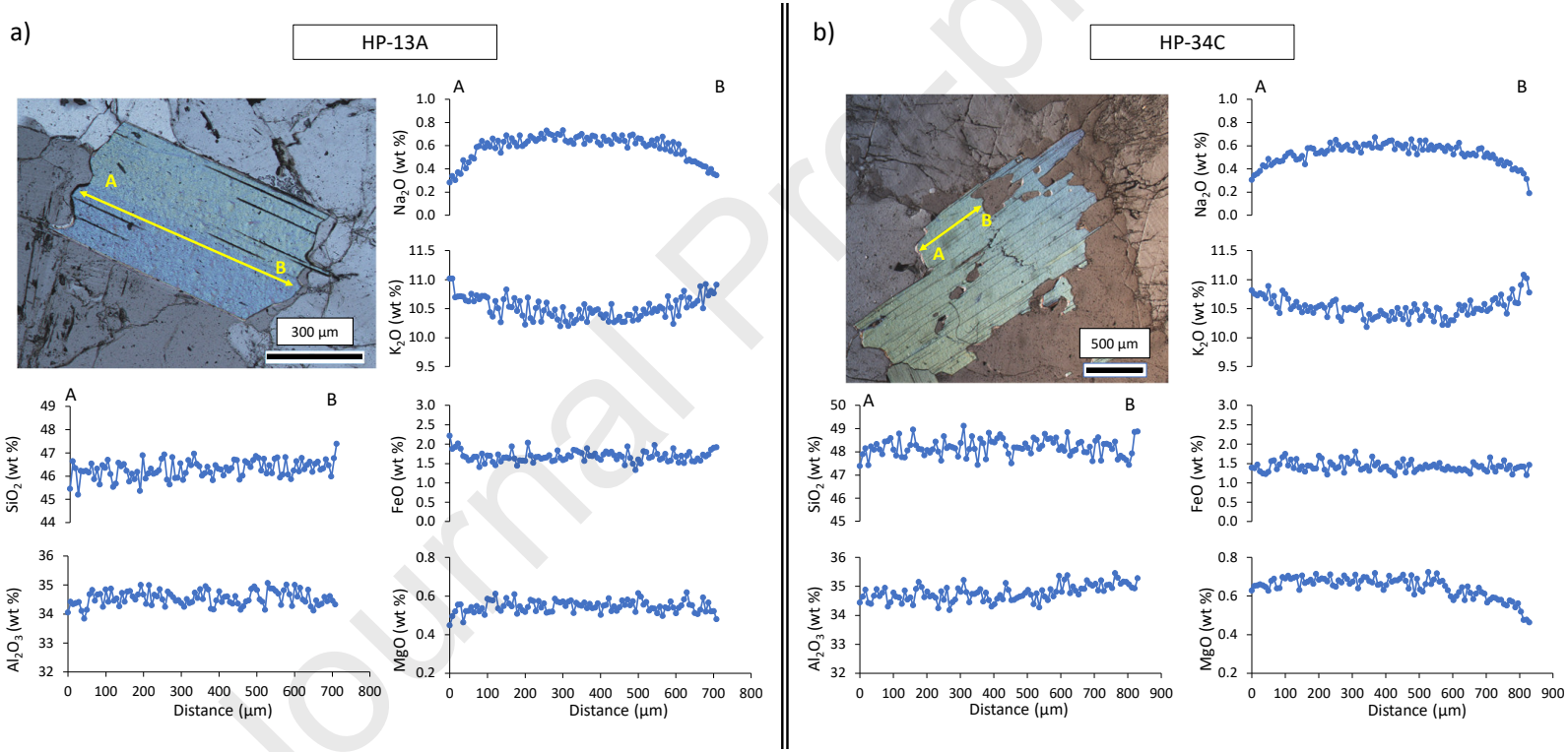

Fig. 11

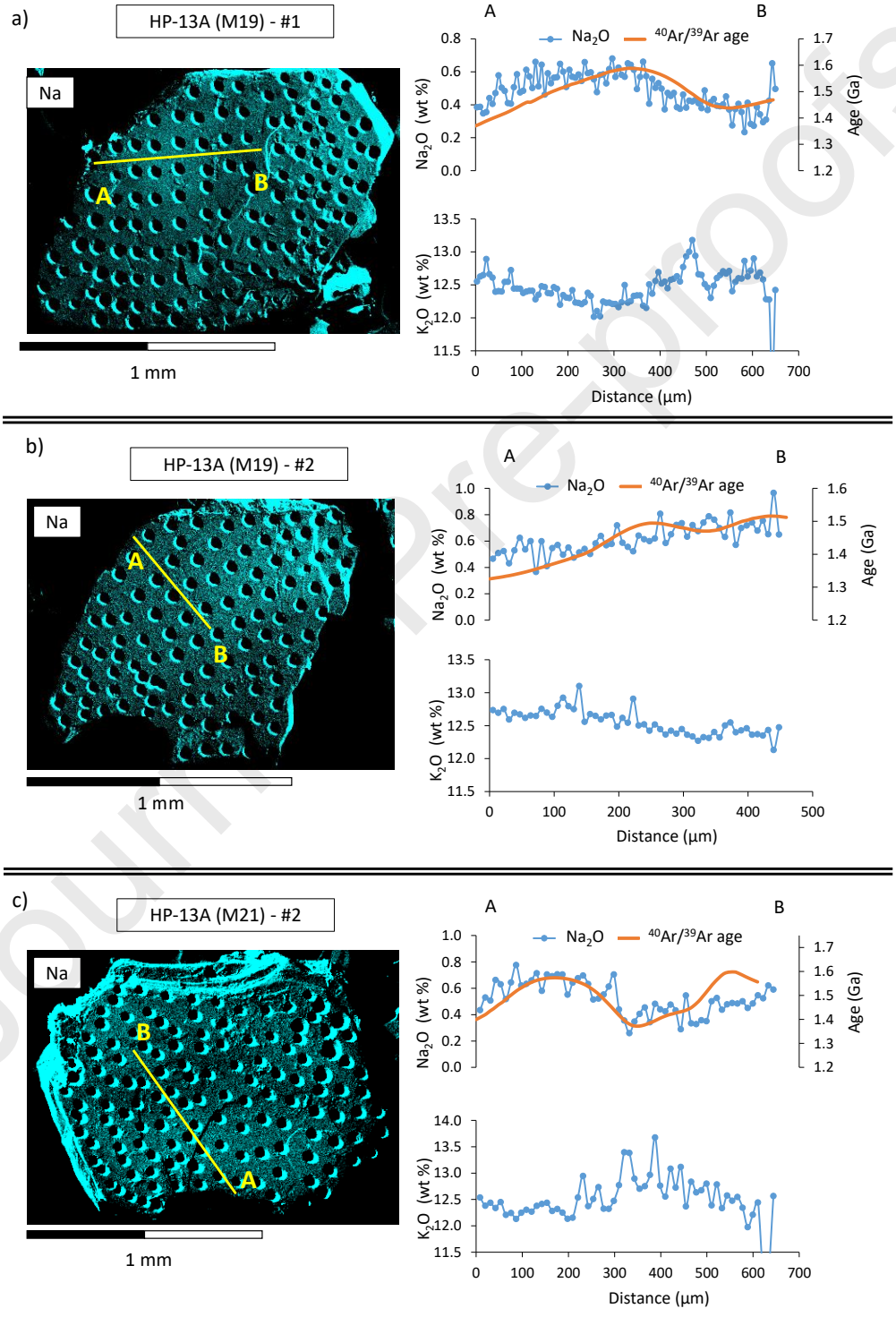
a)
HP-13A (M19) - #1
Na
A
B
1 mm
A
B
Na2O
40Ar/39Ar age
Na2O (wt %)
Age (Ga)
K2O (wt %)
Distance (µm)
b)
HP-13A (M19) - #2
Na
A
B
1 mm
A
B
Na2O
40Ar/39Ar age
Na2O (wt %)
Age (Ga)
K2O (wt %)
Distance (µm)
c)
HP-13A (M21) - #2
Na
B
A
1 mm
A
B
Na2O
40Ar/39Ar age
Na2O (wt %)
Age (Ga)
K2O (wt %)
Distance (µm)

Fig. 12

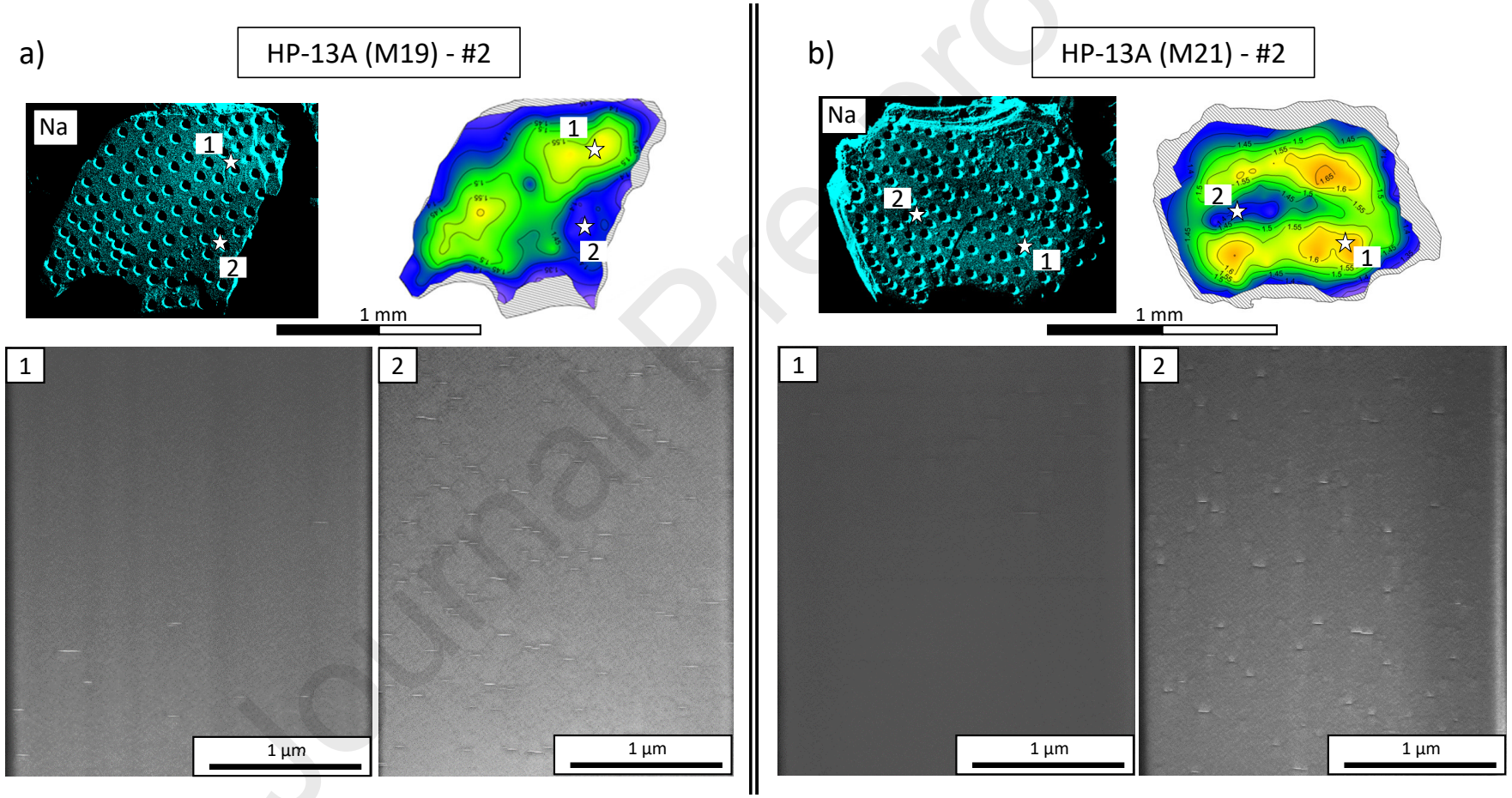

Fig. 12: (Continued)

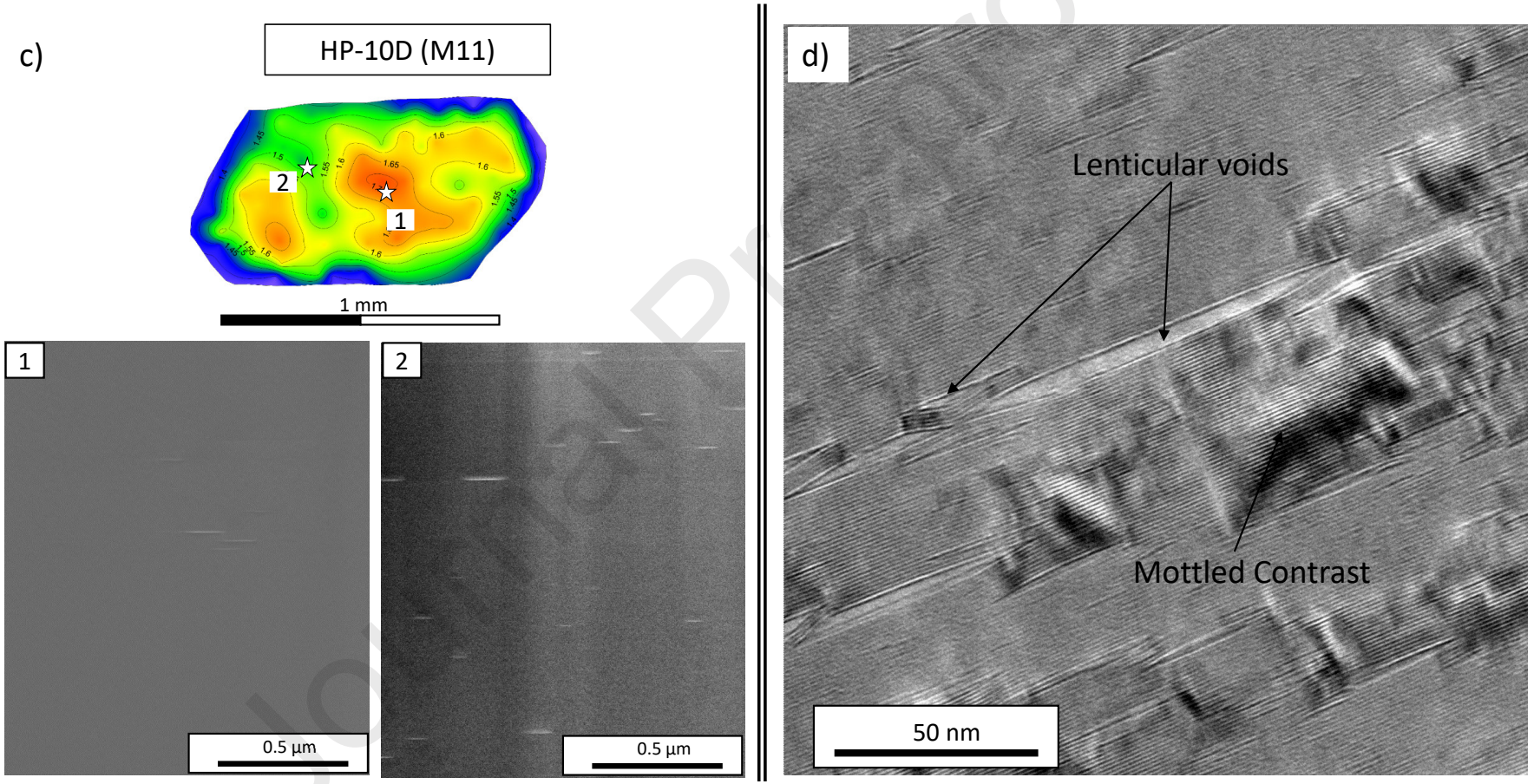

Fig. 13

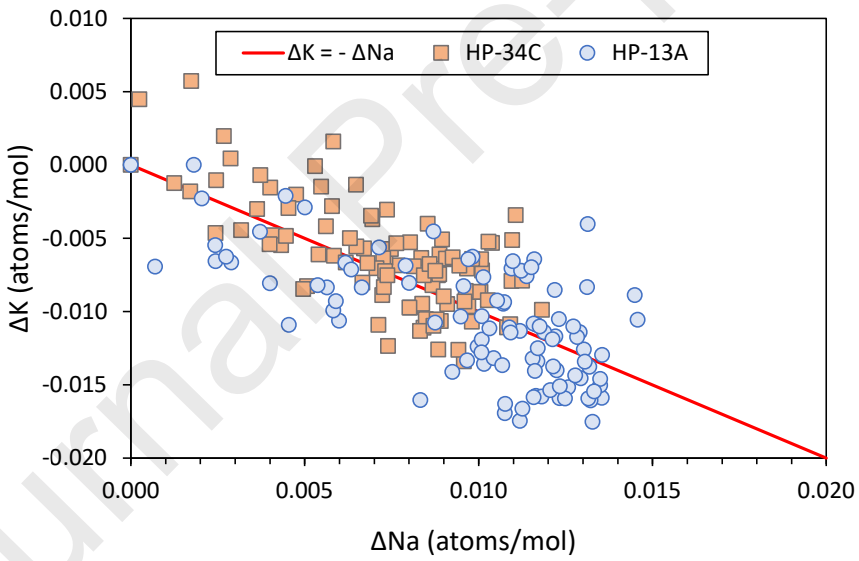

Fig. 14

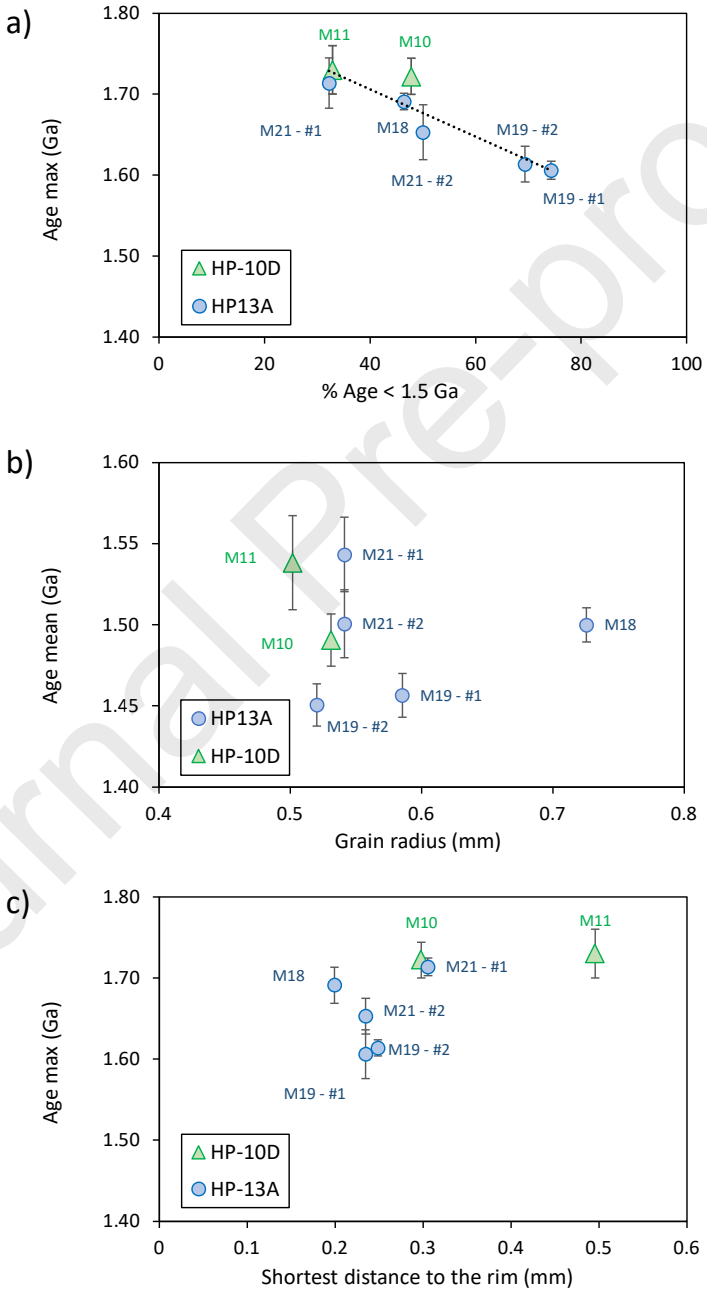

Fig. 15

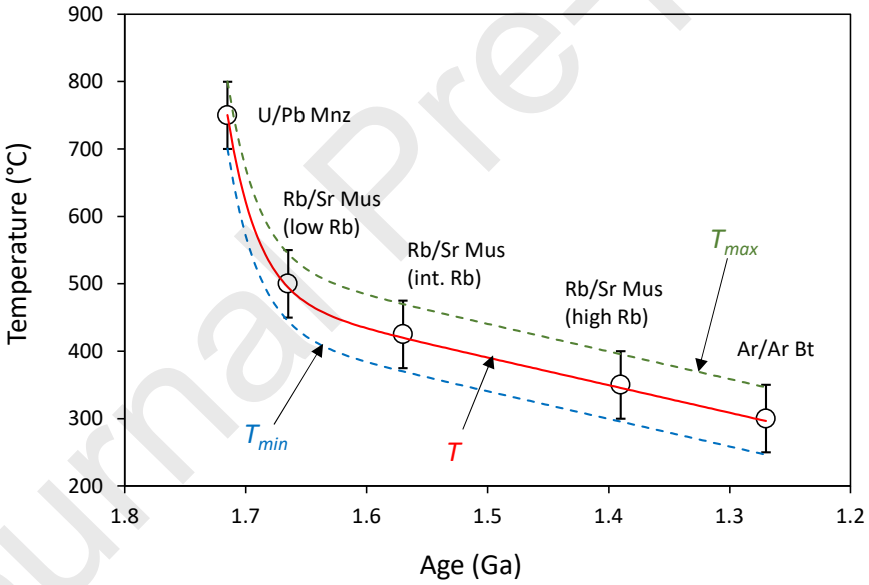

Fig. 16

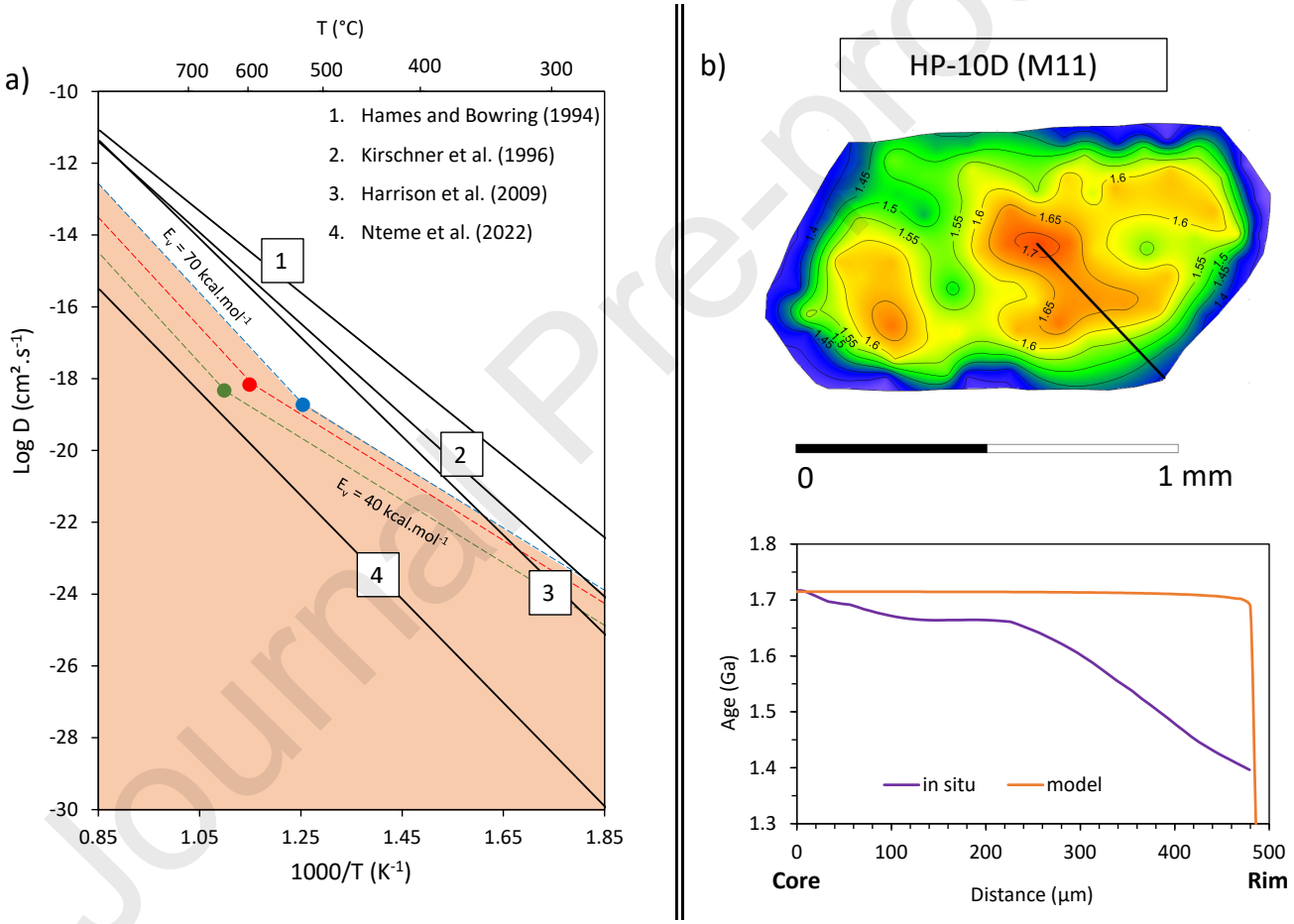

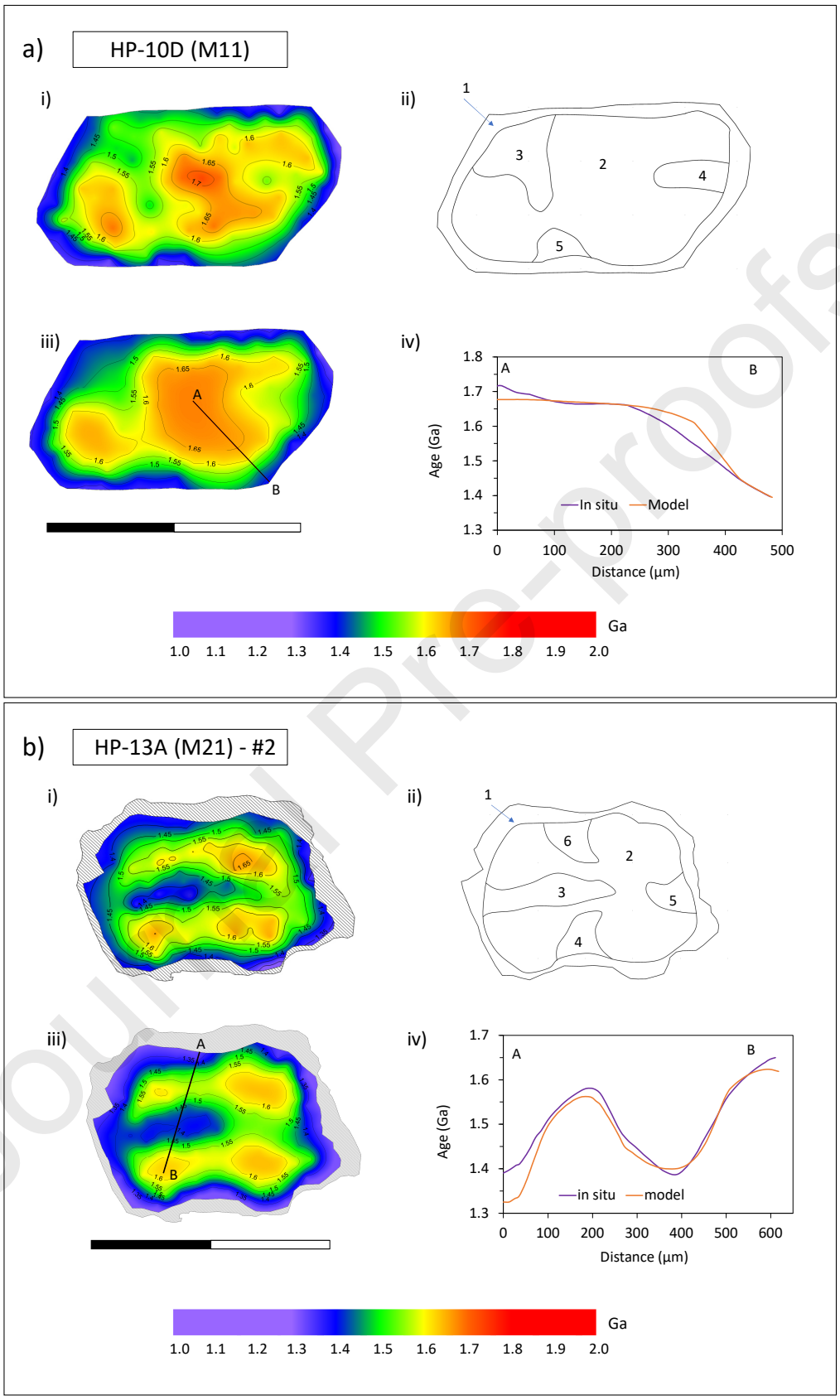
a)
HP-10D (M11)
i)
ii)
1
2
3
4
5
iii)
A
B
iv)
A
B
Age (Ga)
1.8
1.7
1.6
1.5
1.4
1.3
In situ
Model
0
100
200
300
400
500
Distance (µm)
Ga
1.0 1.1 1.2 1.3 1.4 1.5 1.6 1.7 1.8 1.9 2.0
b)
HP-13A (M21) - #2
i)
ii)
1
2
3
4
5
6
iii)
A
B
iv)
A
B
Age (Ga)
1.7
1.6
1.5
1.4
1.3
in situ
model
0
100
200
300
400
500
600
Distance (µm)
Ga
1.0 1.1 1.2 1.3 1.4 1.5 1.6 1.7 1.8 1.9 2.0

Fig. 17

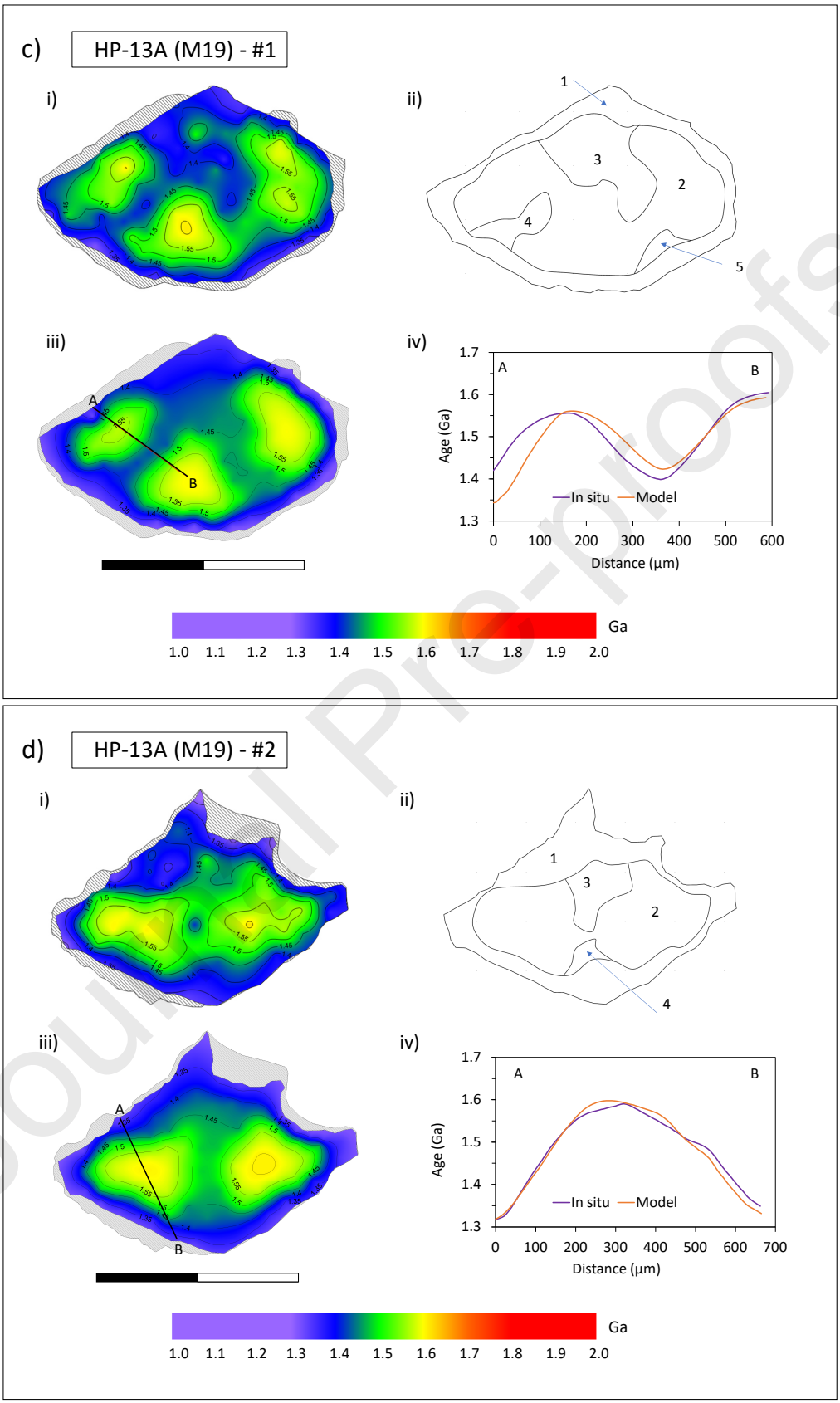

Fig. 17: (Continued)

Fig. 18

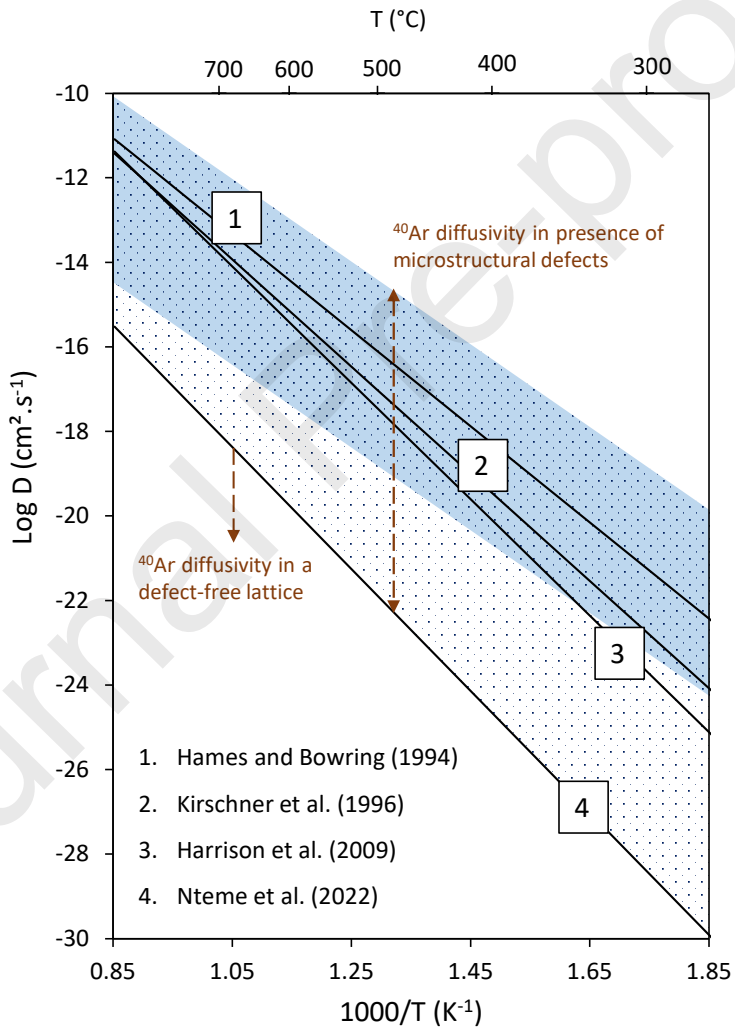

Declaration of interests

☒ The authors declare that they have no known competing financial interests or personal relationships that could have appeared to influence the work reported in this paper.

☐The authors declare the following financial interests/personal relationships which may be considered as potential competing interests: